Primary microfossiliferous chert in the Aptian Barra Velha Formation

KELSEY R. MOORE*·† , ANTOINE CRÉMIÈRE*·‡ , THEODORE M. PRESENT* ,
ANDREW BARNETT§, KRISTIN D. BERGMANN¶, JOACHIM AMTHOR**·†† and
JOHN GROTZINGER*

Division of Geological and Planetary Sciences, California Institute of Technology, Pasadena, CA 91125, USA (E-mail: kmoor101@jh.edu)

†Department of Earth and Planetary Sciences, Johns Hopkins University, Baltimore, MD 21218, USA

‡Geo-Ocean UMR 6538 CNRS- Ifremer-UBO-UBS, Plouzané F-29280, France

§Shell UK, London SE1 7NA, UK

¶Department of Earth, Atmospheric and Planetary Sciences, Massachusetts Institute of Technology, Cambridge, MA 02139, USA

***Shell Brazil Petróleo, Rio de Janeiro 20031, Brazil*

††Division of Earth Sciences and Geography, Rhine-Westphalia Technical University of Aachen, Aachen 52064, Germany

ABSTRACT

The Barra Velha Formation and other Aptian pre-salt deposits record the history of the proto-Atlantic basin and the rifting of Gondwana. Studies have sought to characterize the depositional environment of the basin with a focus on carbonate fabrics and magnesium silicate clays. However, the water chemistry and fluid sources in the basin, the silica cycle, and how the basin evolved over time are not fully constrained. Additionally, current understanding of the microbiota that inhabited this basin is incomplete because microfossils have rarely been identified in pre-salt deposits, especially on the Brazilian margin. This study describes authigenic chert in the Barra Velha Formation that preserves distinct, organic-rich structures and textures. The petrographic relationships between the chert and carbonate suggest that both formed as authigenic phases, but their formation was temporally decoupled. These relationships and δ^{30}Si and δ^{18}O data suggest that chert post-dates the formation and subsequent dissolution of the carbonates, and may have formed from a different fluid. By characterizing the chert–carbonate paragenesis and mechanism of chert formation, this study provides new insights into the fluid sources and complexity of the basin. Together, the results of this research suggest that the chert precipitated as primary, authigenic phases after karstification of the carbonate from a newly introduced, low temperature, freshwater fluid that was chemically distinct from the lake water. The chert preserves organic matter that is compositionally and texturally distinct from the void-filling bitumen associated with the classically studied carbonate facies. Based on the composition and morphologies of organic structures, this is likely primary organic matter and a morphologically diverse microfossil assemblage preserved in place at the time of chert formation. Thus, this early chert provides new insights into the water chemistry, fluid sources and silica cycle in the basin, and represents a unique taphonomic window that helps us characterize the pre-salt basin microbiota.

Keywords Aptian, Barra Velha Formation, chert, microfossil, pre-salt.

INTRODUCTION

The Santos Basin of offshore Brazil hosts a complex sedimentary and volcanic/intrusive fill termed the Aptian 'Pre-salt' that records the rifting of Gondwana and the formation of a proto-Atlantic basin (Moreira *et al.*, 2007; Carminatti *et al.*, 2008; Nakano *et al.*, 2009). The sedimentary portion of the fill – in particular the carbonates – have been the subject of studies aimed at understanding the proto-Atlantic basin and characterizing this depositional environment. In particular, the chemical conditions of the basin, whether it was lacustrine or marine, the sources of water into the basin, and the role of the microbiota in mineral precipitation have been the subjects of broad discussion (Moreira *et al.*, 2007; Terra *et al.*, 2009; Wright, 2012; Wright & Barnett, 2015, 2017, 2020; Chafetz *et al.*, 2018; Pietzsch *et al.*, 2018, 2020; Mercedes-Martín *et al.*, 2019; Azerêdo *et al.*, 2021; Bastos *et al.*, 2022; Carramal *et al.*, 2022). This is related, in large part, to the enigmatic carbonate facies preserved in the pre-salt deposits and the uncertainties surrounding their formation mechanisms. An understudied chert-rich facies in the pre-salt deposits may provide additional insights into the complexity and evolution of the lake chemistry and a more complete picture of the microbiota that inhabited the basin. A key question relates to the timing of chert precipitation and whether it formed syndepositionally with the carbonates.

The Barra Velha Formation (BVF) was deposited during the rift to 'post-rift' or 'sag' phase of rifting (Moreira *et al.*, 2007) and contains some of these chert-rich facies. Like many pre-salt deposits, the BVF is predominantly characterized by carbonate spherulite, shrub, and calcimudstone facies. Some of the distinguishing characteristics are radial fibrous calcite spherules found in the spherulite facies and branching carbonate structures with an internal radiating fabric (the 'shrubs') found in shrub facies. These carbonate fabrics and associated Mg-silicate clays are unique and have undergone an unusual paragenetic and diagenetic history. While still incompletely constrained, many studies suggest that the BVF and other similar pre-salt formations were deposited in an alkaline lake (Wright, 2012; Wright & Barnett, 2015; Pietzsch *et al.*, 2018, 2020; Mercedes-Martín *et al.*, 2019; Carramal *et al.*, 2022). Some have suggested that the carbonate shrubs and spherulites represent microbial buildup structures (Terra *et al.*, 2009; Chafetz *et al.*, 2018) while others suggest that they formed through abiotic processes

(Wright, 2012; Wright & Barnett, 2015). However, whether microbially influenced or not, the carbonate facies do not typically preserve microbial textures or microfossils. Instead, these facies are a main component of the oil reservoir and therefore contain bitumen and oil – thermally mature organic matter introduced into the carbonate deposits after burial. Thus, current understanding of the microbiota, the complexity and distribution of microbial communities, and the role of microbes in mineral formation remains incomplete. Additionally, current models for the chemical conditions of the lake based predominantly on carbonate and Mg-silicate phases likely do not capture the true complexity of the lake system and the potential for multiple different chemical environments and water sources into the basin. In particular, these models typically do not consider potential authigenic chert or any potential biosignatures that it may preserve.

This study describes samples from the BVF that contain synsedimentary or authigenic chert that preserves an important taphonomic window into the microbiota of the pre-salt basin. In particular, this study compares the textures, compositions, and organic material in carbonate facies and previously uncharacterized chert-rich facies in three different wells in the Santos Basin, part of the Brazilian margin of the pre-salt basin. The synsedimentary and diagenetic features in cherts and carbonates are contrasted and key taphonomic differences are characterized across facies and minerals. The authors propose that a subset of the chert-rich samples – which preserve fossil kerogen and potential microfossils – represent a microfossiliferous chert–boundstone facies. The microfossiliferous chert–boundstone formed in spatially isolated environments in which chert and carbonate both represent primary, synsedimentary phases, but the formation of each was temporally decoupled. Characterization of these chert-rich facies and their environment of formation provides a new dimension to the current understanding of the microbiota, water chemistry, fluid sources, and evolution of this ancient basin.

GEOLOGICAL SETTING

The Barra Velha Formation (BVF) is one of a group of formations that were deposited in the Cretaceous rift basin that formed during the breakup of Gondwana. These deposits collectively record the presence of an Aptian alkaline lake (or lakes) developed before the Albian marine incursion and

the opening of the Atlantic Ocean. The BVF lies in the Santos Basin off the coast of Brazil and formed during the syn-rift to sag phase of rifting (Moreira *et al.*, 2007; Wright & Barnett, 2020). It unconformably overlies the Itapema Formation, a bivalve coquina dominated unit deposited in an alkaline lake, and is overlain by the marine evaporites of the Ariri Formation (Wright & Barnett, 2020). Previous studies have interpreted the carbonate facies in the BVF and other pre-salt deposits as alkaline lake deposits (Wright, 2012; Wright & Barnett, 2015; Pietzsch *et al.*, 2018, 2020; Mercedes-Martín *et al.*, 2019; Carramal *et al.*, 2022). Additional work has characterized the facies changes throughout the BVF and suggest that the carbonate spherulite, shrub, and laminate facies formed as decimetre to metre-scale cyclothems that record cycles of lake level rise and fall (Wright & Barnett, 2015). These cyclical carbonate facies dominate the BVF over large areas of the Santos Basin, at least on the structural highs that have been the primary drilling target to date. However, local exceptions occur where thick (decametre-scale), continuous successions of atypical carbonates including grainstone and rudstone facies containing fragments of shrubs, spherulites, and intraclasts are encountered. The thickness of these vertical successions of detrital grain-supported carbonate cannot be readily explained by simple cycles of lake level increase followed by progressive evaporation prior to the next flooding event. Barnett *et al.* (2021, 2018) suggested that grainstone and rudstone facies occur in two distinct structural and stratigraphic settings:

1 Associated with unconformities on the escarpment and dip slopes of tilted fault blocks where a marked thinning of the BVF is evident.
2 Apparent debris aprons adjacent to seismically resolvable mounds that developed on narrow, elongate fault blocks.

The present study describes samples from three drill cores collected across three wells from both the cyclic and mound-dominated successions that capture a range of these atypical carbonate facies as well as rare chert-rich facies. The grainstone facies from these cores may be either peloid–spherulite grainstone or spherulite-dominated grainstone facies that are more heavily altered and show more evidence of physical transport of spherulite grains and other clasts than classically described Mg-silicate clay associated spherulite facies. The shrub-like facies are characterized by distinct fabrics that differ from the more classically described shrub facies present in other parts of the BVF (e.g. Moreira *et al.*, 2007; Terra *et al.*, 2009; Wright, 2012; Wright & Barnett, 2015, 2017, 2020; Chafetz *et al.*, 2018; Pietzsch *et al.*, 2018, 2020; Mercedes-Martín *et al.*, 2019; Azerêdo *et al.*, 2021; Bastos *et al.*, 2022; Carramal *et al.*, 2022). Rather than laminated, bladed or fibrous fabrics, and branching, columnar or fan-like morphologies, these shrubs are often micritized, encrusted, demonstrate some combination of laminated and bladed fabrics, and fall somewhere between branching and columnar morphologies (Rodríguez-Berriguete *et al.*, 2022). Finally, brecciated carbonates as well as clotted carbonate fabrics are present throughout these three cores.

The samples analysed here span stratigraphic intervals of the pre-salt deposits including two cores from the upper BVF (Wells B and C) which lie stratigraphically above the Intra-Alagoas unconformity, and one core from the lower BVF (Well A) which lies stratigraphically below the Intra-Alagoas unconformity but above the Pre-Alagoas unconformity (Table 1; Fig. 1). Well A penetrates a cyclic succession dominated by shrub facies with subordinate intercalated spherulite and laminated calcimudstone facies. Stratigraphically, it samples a *ca* 160 m thick interval in the lower BVF below the Intra-Alagoas unconformity. Well B samples a *ca* 50 m thick interval which straddles the boundary between an overlying cyclic succession and an underlying mound-dominated succession. Well C is from a mound-dominated succession comprising almost exclusively shrub and grainstone facies. Both wells B and C sample the upper part of the BVF above the Intra-Alagoas unconformity. Together, these cores span the Alagoas interval and record any potential associated lake level changes that pre-date and post-date the Alagoas unconformity.

METHODS

Samples analysed in this study include plugs from three drill cores collected in three wells from the Santos Basin. One-inch diameter plugs were extracted from facies of interest and sent to the California Institute of Technology for analyses. A total of 12 plugs were selected from these samples as representative carbonate-rich and chert-rich facies of the cores (Table 1). A portion of each plug was sent to Wagner Petrographic or High Mesa Petrographics to be prepared as 1-inch (2.5 cm) diameter round thin sections. Another portion of each sample was retained for use in Scanning

Table 1. Samples analysed in this study across wells A, B and C with associated sample depth, depth below the base of the salt (BoS) and sample descriptions.

Depositional interval	Well	Sample name	Sample depth (m)	Depth below base of salt (m)	Sample description
SK44	Well A	SPS S1	5301.00	273.8	Clotted carbonte
SK44	Well A	SPS S6	5356.00	328.8	Clotted carbonte
SK44	Well A	SPS S9	5391.00	363.8	Carbonate grainstone
SK44	Well A	SPS S11	5396.00	368.8	Carbonate spherulite
SK44	Well A	SPS S12	5405.00	377.8	Chert-rich
SK44	Well A	SPS S19	5458.00	430.8	Chert-rich
SK46/48	Well B	GDM S1	5207.00	18.7	Carbonate spherulite
SK46/48	Well B	GDM S3	5207.52	19.2	Carbonate stromatolite
SK46/48	Well B	GDM S4	5227.83	39.5	Chert-rich
SK46/48	Well B	GDM S5	5233.51	45.2	Carbonate spherulite
SK46/48	Well B	GDM S6	5239.13	50.8	Carbonate shrub
SK46/48	Well B	GDM S8	5259.31	71.0	Chert-rich
SK46/48	Well C	D	5166.25	65.7	Chert-rich
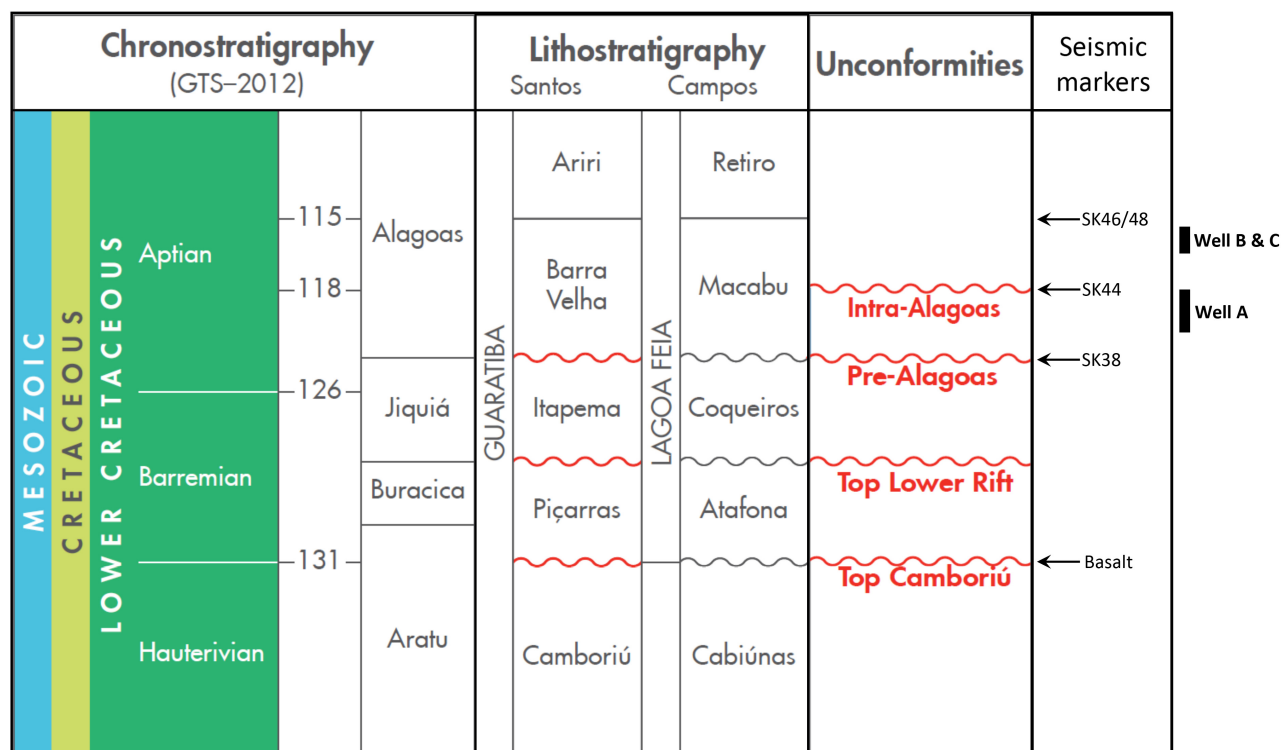
Fig. 1. Lower Cretaceous stratigraphic chart for the Santos and Campos Basin (after Moreira *et al.*, 2007).

Electron Microcopy (SEM) so that organic material could be identified without organic contribution from epoxy used in the thin section preparation. Each sample was analysed using SEM with energy dispersive X-ray spectroscopy (EDS), transmitted and reflected light microscopy, and secondary ion mass spectrometry (SIMS). These combined analyses were used to characterize petrographic relationships between chert and carbonate, to identify and characterize organic matter and organic-rich structures associated with both phases, and to determine the $\delta^{30}Si$ and $\delta^{18}O$ of the chert. See supplemental methods for full details of each analysis (Appendix S1).

RESULTS

Carbonate facies

Facies description
The BVF contains a mixture of carbonate facies across the three cores investigated in this study (Figs 2 and 3; Table 1). In Well A, the dominant carbonate facies are carbonate peloid–intraclast grainstone facies (Fig. 3A), carbonate spherulite-rich grainstone facies, and intraclast grainstone carbonate facies characterized by clotted carbonate fabrics (Fig. 3B). In Well B, facies include carbonate spherulite–intraclast grainstone facies (Fig. 3C), carbonate stromatolite facies (Fig. 3D), and carbonate shrub facies (Fig. 3E). In Well C, carbonate shrub facies are dominant. Below, the textural and compositional features of each of these facies are described.

The main difference between spherulite-rich grainstone facies (Figs 2A and 3C) and peloid–intraclast grainstone facies (Fig. 3A) is the dominance of calcite spherules with radial fibrous fabrics versus peloids and shrub fragments. In both types of grainstone facies, the spherules and other carbonate grains are compacted and sutured with concavo–convex grain boundaries and are frequently rimmed by dolomite (Fig. 3C). The intergranular space is typically filled by blocky, euhedral quartz cement, dolomite cement, or both, and secondary porosity is present throughout (Fig. 3A and C). The radial fabric of the spherules is still largely apparent, but both the spherules and other carbonate grains have been partially replaced by quartz and dolomite, overprinting the fabric to varying degrees across grains within a given sample (Fig. 3A and C).

Clotted carbonate textures are predominantly present in carbonate facies from Well A. The carbonate throughout the samples is interconnected with an internal microclotted texture with mottled tan and grey carbonate and abundant pore space between clots (Fig. 3B). The majority of the compacted intraclasts in the peloid–intraclast grainstone facies from this well have a similar internal clotted texture. Some grains have a fibrous or bladed fabric, though the orientation of the fabric is random and shows no uniform geopetal direction (Fig. 3A). The clotted carbonate fabrics and carbonate grains are replaced to varying degrees by dolomite and quartz, and both quartz and dolomite cement are present in the intragranular space, though dolomite is the dominant cement (Fig. 3B).

Stromatolite facies (Figs 2B and 3D) are characterized by alternating laminae with two distinct carbonate textures. One type of lamination is characterized by a peloidal microtexture with carbonate peloids surrounded by quartz and dolomite cements (Fig. 3D). These layers alternate with layers of fibrous calcite cement. The fibrous fabric of the calcite is perpendicular to lamination in some layers, but some layers display fibrous fabric oriented both perpendicular and parallel to lamination (Fig. 3D). The calcite in these facies has a cloudy appearance and contains microdolomite inclusions, a potential indicator that the original mineralogy was high magnesium calcite (HMC; Lohmann & Meyers, 1977). The carbonate peloids and the fibrous calcite cement are replaced to varying degrees by quartz and abundant secondary porosity is present within the peloid-rich laminae and between peloid laminae and fibrous calcite laminae (Fig. 3D).

Shrub facies are characterized by branching and vertically aggregating clusters of bladed calcite (individual shrubs) with the internal bladed fabric oriented perpendicular to bedding (Figs 2C and 3E). The shrubs show evidence of internal banding, perhaps representing generations of vertical growth (Fig. 3E). These 'shrub' facies are slightly atypical compared to many previously described 'shrub' facies and most closely resemble the Type 4 shrubs characterized by Rodríguez-Berriguete *et al.* (2022). Like the calcite spherules and intraclasts, shrubs may be partially micritized or replaced by quartz and dolomite. In most samples, primary inter-particulate and inter-shrub pore space is filled by sparry calcite and blocky, euhedral quartz cement (Fig. 3E).

Organic matter in carbonate facies
Secondary pore space is abundant across these carbonate facies and is typically filled by late
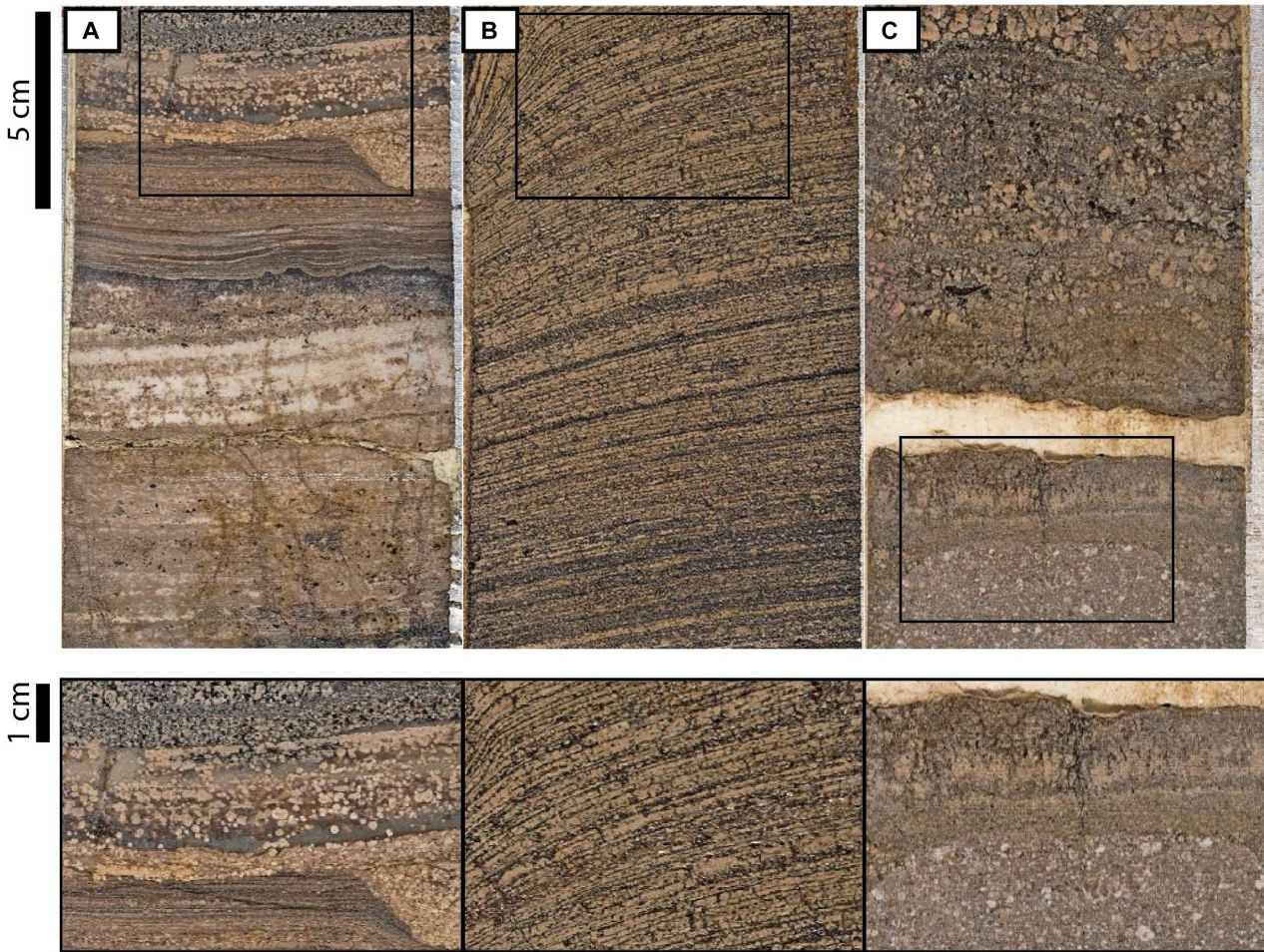
Fig. 2. Representative core photographs of major carbonate facies (bottom panel depicting zoomed in regions of the main fabrics). These include: (A) spherulite-rich grainstone facies; (B) stromatolite facies; and (C) 'shrub' facies with branching carbonate shrubs.

carbonate and quartz cements. Many of the carbonate samples contain little to no organic matter. However, in samples that do contain organic matter, the organic matter is localized to secondary pore spaces and is not preserved within the carbonate grains or cements, evidenced by light microscopy as well as SEM images and EDS maps (Figs 3C, 3D and 4). The organic matter – which has a dense, dark appearance in both transmitted light and in BSE images and apparent fracture networks reminiscent of brittle fracturing – is often embedded with quartz, dolomite, and calcite grains ranging in size from nanoscopic up to *ca* 30 μm in diameter (Fig. 4). The EDS spot analyses show that pore-filling organic matter has a low O/C ratio and is predominantly composed of carbon and oxygen with only minor S and trace amounts of Na, Cl, Mg and Ca (Fig. 4).

Chert-rich facies

Facies description

Five samples from the BVF display key differences that set them apart from the carbonate facies (Table 1). Microcrystalline chert is a prominent component of these samples, comprising >25% of each sample on average, surrounding the carbonate and filling most of the intergranular space (Figs 5 and 6). The crystals in these regions range in size but are <20 μm and have irregular grain boundaries and undulose extinction (Fig. 6A to D). At the core scale, these samples display brecciation of carbonate with poorly sorted, angular intraclasts of variable sizes from *ca* 10 mm up to *ca* 2 cm (Figs 5A, 5B, 6A and 6B), mosaic fracture networks (Fig. 5C), and solution-enhanced fractures and secondary porosity filled with silica
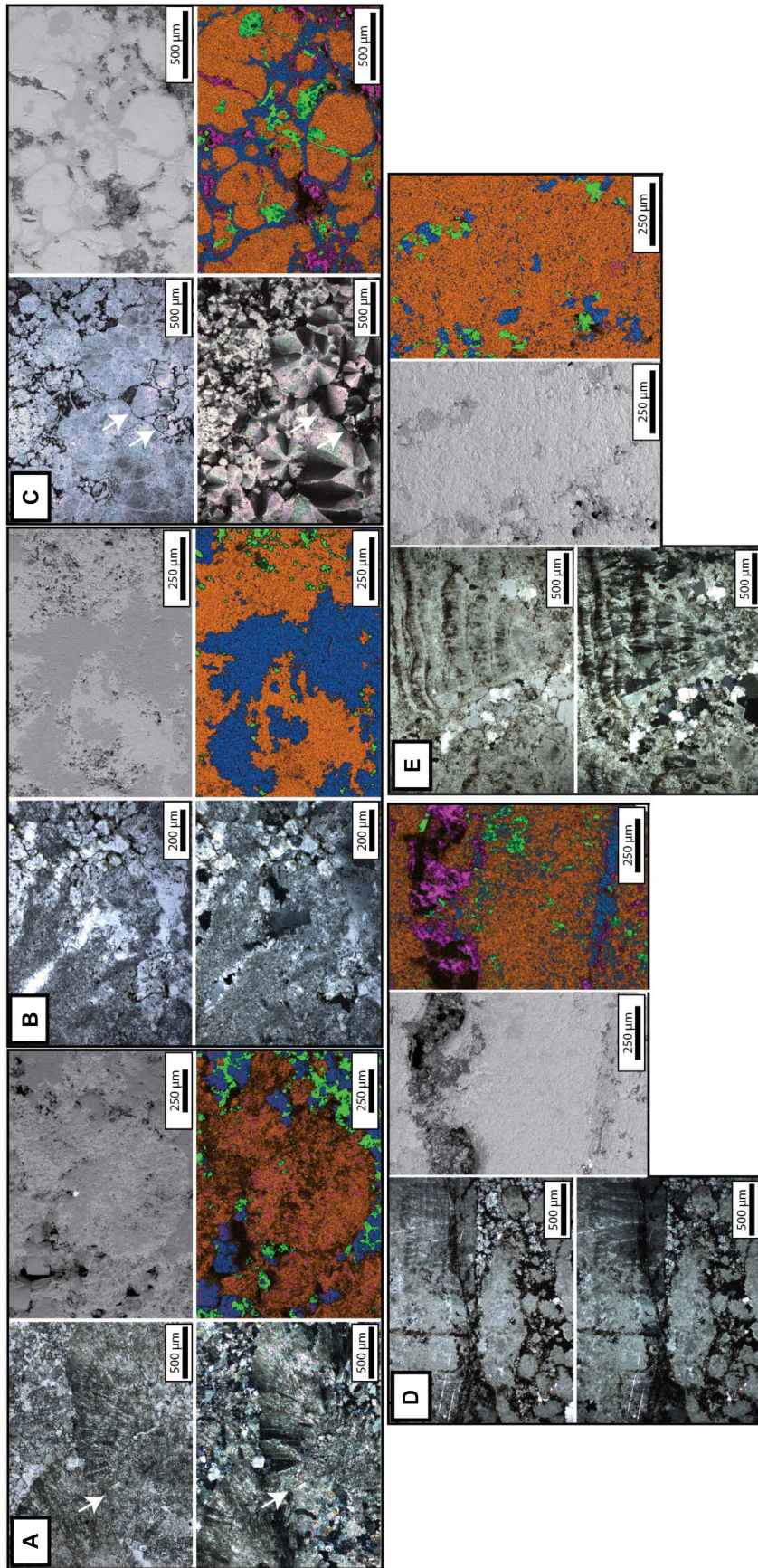
Fig. 3. Microscale textures of representative carbonate facies. For each plate, the left panels show plane plane polarized (top) and cross-polarized (bottom) light microscope image and the right panels show backscatter electron (BSE) images (top) and energy dispersive X-ray spectroscopy (EDS) elemental overlays (bottom). In EDS overlays; orange = Ca, blue = Mg, green = Si, and pink = C. (A) Peloid–intraclast grainstone with compacted, sutured intraclasts (white arrow) including a mixture of shrub fragments, peloids, and spherules surrounded by quartz and dolomite cement. (B) Clotted carbonate fabric partially replaced by silica and surrounded by dolomite cement. (C) Spherule-rich grainstone with compacted and sutured spherules and peloids (white arrows) that are partially replaced by silica and surrounded by dolomite. Grains are surrounded by dolomite rims and silica cement, and secondary porosity is filled with organic matter. (D) Stromatolite with alternating peloid rich laminae (lower portion of light microscope images) and fibrous calcite cement laminae (upper portion of light microscope images), both partially replaced by silica and dolomite. Secondary porosity between laminae is filled with organic matter. (E) Carbonate shrubs with layers of bladed calcite and 'growth bands'. Shrubs are partially replaced by silica and dolomite and are surrounded by quartz and dolomite cement.
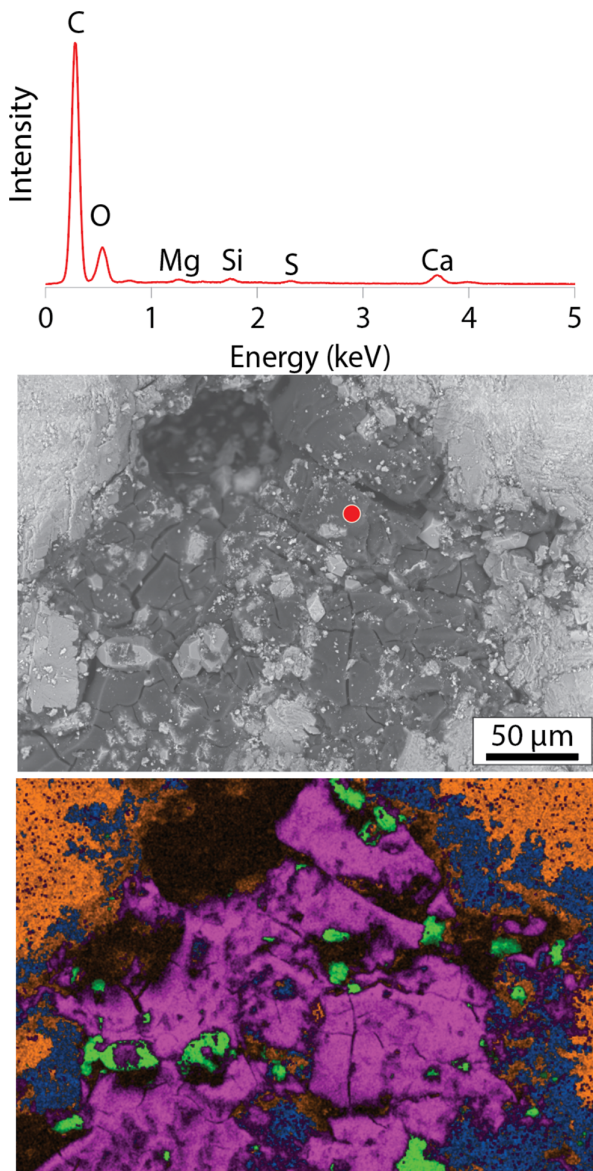
Fig. 4. Chemical composition and microscale textures of void-filling organic matter from a spherulite-rich grainstone (Fig. 4C). Backscatter electron (BSE) image shows that organic matter is dark and dense and shows fracture networks. EDS spot analyses (red dot) show that the organic matter has a low O/C ratio and energy dispersive X-ray spectroscopy (EDS) maps highlight the quartz and carbonate grains embedded in the organic matter.

(Fig. 5C). These features are present below sharp surfaces, with enhanced secondary porosity and dissolution in the carbonates which tend to elongate horizontally along bedding planes (Fig. 5C). The carbonate associated with silica in these samples displays three dominant fabrics.

The first fabric is carbonate intraclasts bound within the chert matrix (Figs 5A, 5B and 6A to D). The intraclasts are generally composed of microcrystalline calcite that lacks internal fabrics (Fig. 6A and B), though some display faint radial and bladed fabrics possibly representing remnant shrub and spherulite fabrics. However, these fabrics are randomly oriented and the intraclasts are not connected to other carbonate regions (Figs 6C, 7A and 7B). The carbonate intraclasts in these samples show little evidence of suturing or other compaction textures and are only occasionally in contact with other carbonate intraclasts (Fig. 6A to D). Instead, they are typically surrounded by microcrystalline chert. Intraclasts show variability in rounding ranging from rounded to angular and have sharp boundary contacts with the microcrystalline chert that surrounds them (Fig. 6A to D). Some intraclasts have rough, irregular edges with a spongy appearance and are encrusted by organic material (for example, Fig. 6A and B).

The second fabric is clotted carbonate bound within the microcrystalline chert matrix. The clotted carbonate may be interconnected or present in isolated patches and is surrounded by microcrystalline chert (Figs 6A, 6B and 7A to C). These carbonate patches sometimes have hints of a branching shrub-like appearance, though these are randomly oriented (Fig. 7A). More frequently, the carbonate is microcrystalline and composed of mottled tan and grey toned mesoclots (*ca* 1 to 3 mm) diffusely distributed throughout the carbonate (Figs 6A, 6B and 7B). These clotted carbonate regions have a spongy appearance created by microporosity concentrated around the edges of the carbonate patches and irregular, ragged boundaries and are in sharp contact with the surrounding chert (Figs 6B and 7B). Like the intraclasts, some clotted and shrub-like regions are encrusted by organic material and show evidence of microboring, though the carbonate itself does not preserve organic material (Figs 6B and 7A). The chert in these samples also sometimes displays a diffuse, microclotted texture created by mottling of darker and lighter toned chert (Figs 6B, 6D and 7A to C). In contrast to the carbonate, the microclotted fabric and colour differences in the chert are created by clotted organic textures.

The final fabric is a shrub-like carbonate texture within a microcrystalline chert matrix (Fig. 7C). Rather than carbonate grains and clotted carbonate textures, carbonate shrub fabrics are characterized by branching shrubs
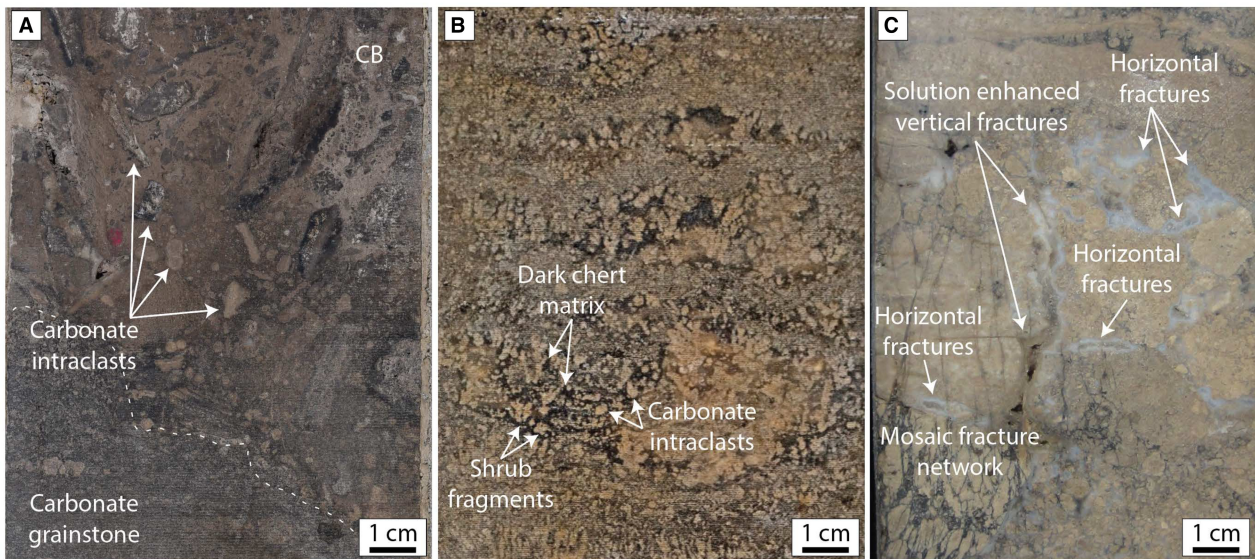
Fig. 5. Photographs of representative chert-rich cores highlighting the chert-carbonate relationships and karst features. (A) Brecciated carbonate with poorly sorted, angular to rounded carbonate intraclasts surrounded by a chert matrix. The base of the breccia has a sharp contact with the underlying carbonate grainstone. (B) Chert-rich carbonate with shrub fragments and other carbonate intraclasts surrounded by a dark chert matrix. (C) Chert-rich carbonate with mosaic fracturing and solution enhanced fractures that run both horizontally and vertically and are filled with microcrystalline chert.

oriented in a generally uniform up direction. These shrubs have a bladed fabric and display some replacement by quartz and dolomite. Importantly, the abundant inter-shrub space is filled with a microcrystalline chert (Fig. 7C). In addition to the connected shrub fabrics that appear to be in place, fragments of shrubs and occasional clotted carbonate intraclasts are also present between the shrubs, surrounded by microcrystalline chert (Fig. 7C). The chert appears to pre-date any compaction or compression of the carbonate textures.

Silica that surrounds and encrusts the carbonate is sometimes present in the form of a chalcedony or microcrystalline chert rims followed by a second generation of chert that fills the remainder of the space between grains and clotted fabrics (Figs 6A and 7B). In some cases, patches of clotted chert display a second generation of chert or chalcedony around the rim followed by successive generations of rims – either in the form of chert bands or randomly distributed microcrystalline chert crystals surrounding the initial bands – filling the remainder of the space (Fig. 6D). Importantly, early, microcrystalline chert rims overgrow, rather than cross-cut or replace, the pre-existing carbonate textures (Fig. 7A and B).

These carbonate textures include corroded clast edges or microbored shrub branches (Fig. 7A and B). Further, while chert commonly contains fluid inclusions and organic carbon inclusions, inclusions of carbonate minerals other than larger carbonate intraclasts were not observed.

Across these chert-rich samples, coarsely crystalline euhedral quartz is present alongside the microcrystalline chert, both as void-filling cement (Fig. 7C) and in veins that cross-cut carbonate and microcrystalline chert. In some samples, chalcedony lines pores that are ultimately filled with the coarse euhedral quartz. The different textures of the microcrystalline chert and the more coarsely crystalline veins and void-filling cements, the cross-cutting relationships of the veins and the microcrystalline chert, and the lack of compaction features in the carbonate all suggest that the microcrystalline chert represents the earliest generation of silica and pre-dates burial and compaction of the carbonate.

Organic matter in chert-rich facies

The silica in all five chert-rich samples contains varying amounts of organic matter and potential microfossils. In all samples, the general texture and appearance of the organic matter, as well as
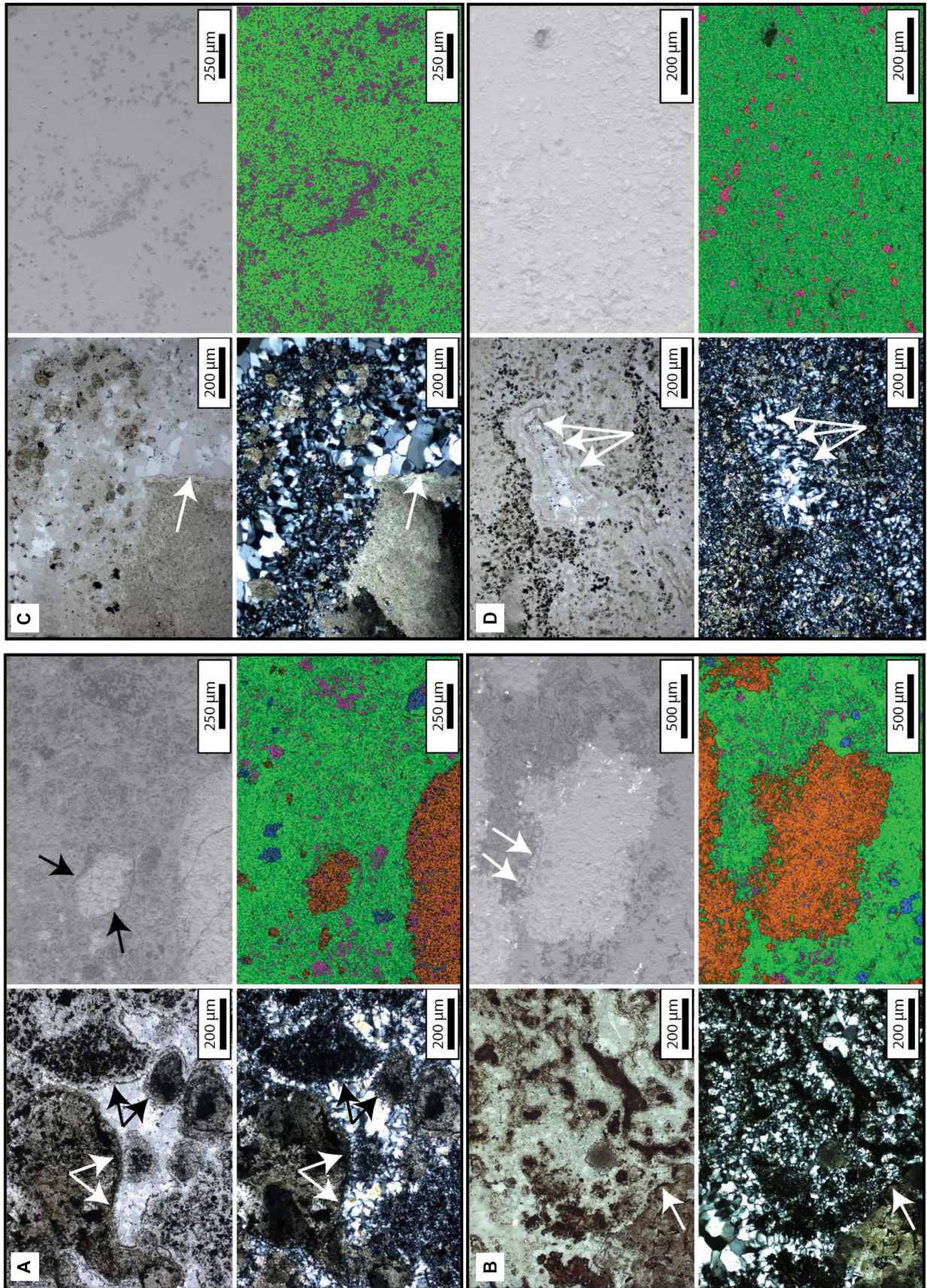
Fig. 6. Microscale textures of representative chert-rich samples. For each plate, the left panels show plane (top) and cross (bottom) polarized light microscope image and the right panels show backscatter electron (BSE) images (top) and energy dispersive X-ray spectroscopy (EDS) elemental overlays (bottom). In EDS overlays; orange = Ca, blue = Mg, green = Si, and pink = C. (A) GDM S8; Rounded to angular carbonate intraclasts in a microcrystalline chert matrix. Some intraclasts are encrusted by organic material (white arrows) and some are surrounded by generations of microcrystalline chert rims (black arrows). (B) GDM S4; Carbonate grains that lack internal fabric within a chert matrix. Carbonate is encrusted with organic material (white arrows) and has rough, irregular edges creating a spongy microtexture. (C) SPS S12; Carbonate intraclast with internal bladed fabric and sharp contact (white arrows) with the surrounding microcrystalline chert. (D) SPS S19; Microcrystalline chert with abundant organic matter and a microclotted appearance created by mottling of light and dark tan to grey-toned chert. Chert shows multiple generations of growth (white arrows). Microcrystalline chert in all samples contains abundant organic matter in the form of <30 μm spheres (dark grey in BSE image, pink in EDS overlays).

its composition, are similar. Rather than the dense, dark material localized to pore spaces in the carbonate facies, the organic matter in the chert-rich facies is preserved within the microcrystalline chert matrix and has a 'fluffy' appearance and lighter tone in BSE images (Fig. 8). The EDS spot analyses reveal that this organic matter has a higher O/C ratio compared to the void-filling organic matter in carbonate facies and has higher cation content (Na, Mg and Ca) and more organic P and S (Fig. 8). This chert-bound organic matter is present in a variety of forms throughout the samples, including: (i) clots of organic matter; (ii) diffuse, clotted organic textures; (iii) wispy, branching textures; and (vi) a morphologically diverse group of spherical organic-rich structures that may represent microfossils (Fig. 9).
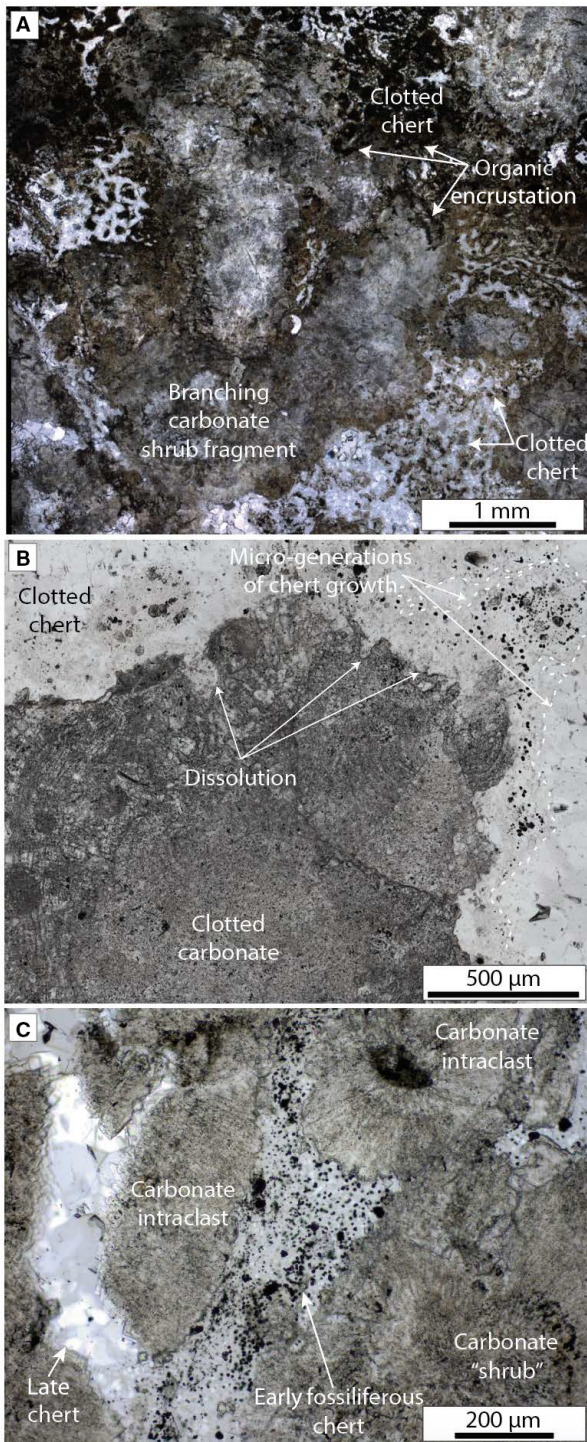
Samples GDM S4 and S8 contain the greatest diversity of organic textures and potential fossil morphologies, though distinct morphologies and organic matter are present in all chert-rich samples (see Table 2 and supplemental results for detailed descriptions of microfossil morphologies). In samples GDM S4 and S8, regions of the microcrystalline chert are often filled with diffuse organic matter, resulting in a dark tan to brown colouration of the chert. Organic matter is often present as either diffuse or dense clots (Figs 7A and 9A to D) that create the clotted microfabric in the chert described in the *Chert-rich facies* and *Facies description* sections. In other regions, organic matter is concentrated into wispy strands that splay into multiple tendrils (Fig. 9B). In some samples, the microcrystalline chert has a more transparent appearance with lower total organic content, though faint hints of diffuse, clotted organic textures generate a similar clotted microfabric in the chert in these samples, as well

(Figs 6C, 6D, 7B, 7C and 9C). Within the organic-rich regions and in regions of microcrystalline chert with lower overall organic content, several potential fossil morphotypes are preserved in the chert (for example, Fig. 9C to E; Table 2; see supplemental results for detailed morphological descriptions).

Geochemical characterization of chert

Chert-rich samples from Wells A, B and C were analysed using SIMS to determine the δ^{30}Si and δ^{18}O of the chert. The oxygen and silicon isotope analyses revealed δ^{18}O values between 29.1‰ and 41.0‰ and δ^{30}Si values between −0.5‰ and 4.5‰ for the microcrystalline chert (Fig. 10). For both isotopes, there is a noticeable skew towards lighter values for samples from the stratigraphically older Well A core [average δ^{18}O = 34.6 ± 2.1‰ SD, $n = 46$ on six different regions of interest (ROIs) and δ^{30}Si = 1.0 ± 0.8‰; $n = 15$ on three different ROIs] and towards heavier isotopic values for the samples from the stratigraphically younger Well B and C cores (average δ^{18}O = 36.9 ± 1.8‰, $n = 111$ on 13 different ROIs and δ^{30}Si = 2.5 ± 1.0‰, $n = 82$ on 14 different ROIs). Averages calculated for the multiple measurements per core (two different samples for Well A and three for Wells B and C) yield standard deviations which consistently decrease with increasing number of analyses and are close to the estimated analytical precision from standard analyses.

Using the equation from Sharp *et al.* (2016), δ^{18}O values were used to calculate temperature of formation for the chert precipitating in equilibrium with water (Fig. 11). To cover the most plausible endmember oxygen isotopic compositions of water, from rainwater to a strongly evaporated lake, the present study assumes a range

Fig. 7. Key fabrics and petrographic relationships in chert-rich samples. (A) GDM S4; a branching shrub fragment encrusted by organic material and surrounded by microcrystalline chert matrix. The chert contains abundant organic matter and has a microclotted appearance created by mottling of light and dark-toned chert and organic material. (B) SPS S12; clotted carbonate with some hints of faint fibrous fabric and ragged, irregular grain boundaries highlighting dissolution of the carbonates. These boundaries have sharp contacts with a first generation of microcrystalline chert that overgrows the carbonate and is followed by a second generation, both of which have a microclotted appearance and preserve organic matter. (C) GDM-D; A portion of an in place, branching carbonate shrub (lower right) and various other carbonate intraclasts surrounded by microcrystalline chert containing organic matter and potential microfossils. Adjacent to this early chert is a later generation of coarsely crystalline, void-filling quartz.

representative of modern precipitation, the temperature of formation of the chert was of $15\pm_6^7$°C for Well A and $8\pm_5^6$°C for Wells B and C. Estimates based on carbonate clumped isotopes measurements from the BVF suggest that the lake water in the Santos Basin ranged from 1.9 and 4.9‰ VSMOW (Lawson *et al.*, 2023). Using the heavier end member fluid $\delta^{18}O$ (5‰) of the lake water, the temperature of formation of the chert was of $54\pm_9^{10}$°C for Well A and $T = 44\pm_7^8$°C for Wells B and C. Based on these calculations, the temperature of formation for the chert was below 54°C and above 8°C with a range of possible temperatures between these depending on the source of the fluid or mixing of fluid sources.

DISCUSSION

Silica paragenesis and syndepositional authigenic chert

The BVF records multiple generations of both carbonate and silica precipitation during deposition and subsequent diagenesis, reflecting the complex history of the proto-Atlantic basin. Identification of the earliest of these phases is important because they record information about the lake water chemistry, physical and geochemical processes, and the biosphere in this ancient basin. Much of the past work on the pre-salt deposits has focused on the carbonates, especially the shrubs and spherulites which are
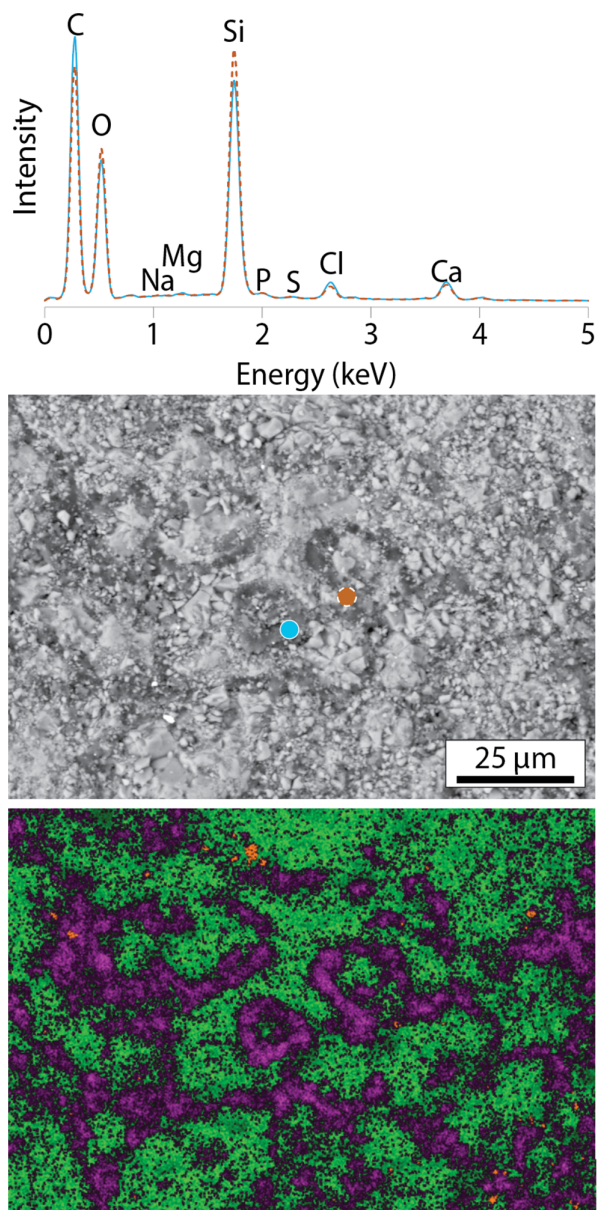
of water $\delta^{18}O$ from −5 to 5‰ Vienna Standard Mean Ocean Water (VSMOW). In the tropical zone at low altitude, the rainfall $\delta^{18}O$ values typically range between −7‰ and −2‰ VSMOW (Bowen & Wilkinson, 2002). Assuming a light end member $\delta^{18}O$ value of −5‰ VSMOW,

Fig. 8. Chemical composition and microscale textures of organic matter in chert-rich facies. Backscatter electron (BSE) image shows that organic matter has a 'fluffy', amorphous appearance and is present both as amorphous clots and as organic-walled, circular structures. Energy dispersive X-ray spectroscopy (EDS) spot analyses (blue and orange dots) show that the organic matter has a high O/C ratio as well as higher S and P compared to the organic matter in Fig. 4. EDS maps highlight the circular cross-section morphology of the organic-walled structures. In EDS maps; green = Si, pink = C, orange = Ca.

interpreted as primary precipitates (Moreira *et al.*, 2007; Terra *et al.*, 2009; Wright, 2012; Wright & Barnett, 2015, 2017, 2020; Chafetz

et al., 2018; Pietzsch *et al.*, 2018, 2020; Mercedes-Martín *et al.*, 2019; Azerêdo *et al.*, 2021; Bastos *et al.*, 2022; Carramal *et al.*, 2022; Tonietto *et al.*, 2023). The majority of the silica in pre-salt deposits, in contrast, has been attributed to late diagenetic processes (Wright, 2012; Wright & Barnett, 2017, 2015; Pietzsch *et al.*, 2020; Azerêdo *et al.*, 2021) or hydrothermal processes (Lima & De Ros, 2019; Sartorato *et al.*, 2020), with some exceptions including early silica nodules in the calcimudstone deposits from the BVF thought to represent a flooding event (Wright & Barnett, 2015, 2020). Earlier studies also investigated different generations of chert from the African margin of the pre-salt basin and identified rare occurrences of pre-compaction silica precipitation associated with brecciated carbonates and microbial buildup structures with clotted microfabrics (Saller *et al.*, 2016; Teboul *et al.*, 2019) similar to the chert that is described in this study. Those studies suggest that the chert precipitated from the lake. However, early generations of chert remain generally understudied throughout the pre-salt deposits, especially on the Brazilian margin, and the water chemistry, fluid sources and mechanisms of authigenic silica precipitation are not fully constrained. Importantly, it is possible that the chert and carbonate formed from two different fluids. Further characterization of these early generations of chert is therefore key to understanding the depositional environment and the evolution of the lake.

The chert-rich samples analysed in this study contain an early generation of microcrystalline chert associated with carbonate intraclasts, clotted carbonate fabrics, and carbonate shrub fabrics that does not fit within the late diagenetic models of silicification. The lack of compaction features in the chert-bound carbonate suggests that the microcrystalline chert pre-dates burial and compaction. Furthermore, the preservation of primary organic matter, delicate microbial fabrics, and potential microfossils (Figs 6, 7, 8 and 9) suggests that this chert is syndepositional. The preservation of such delicate organic textures and potential microfossils is a taphonomic process that requires rapid and early precipitation of silica (Knoll *et al.*, 2013). The microcrystalline nature of the chert, the irregular crystal boundaries, and the undulose extinction are also consistent with early diagenetic or primary formation (Maliva *et al.*, 2005). This is further supported by the textural relationships between the chert and carbonate.
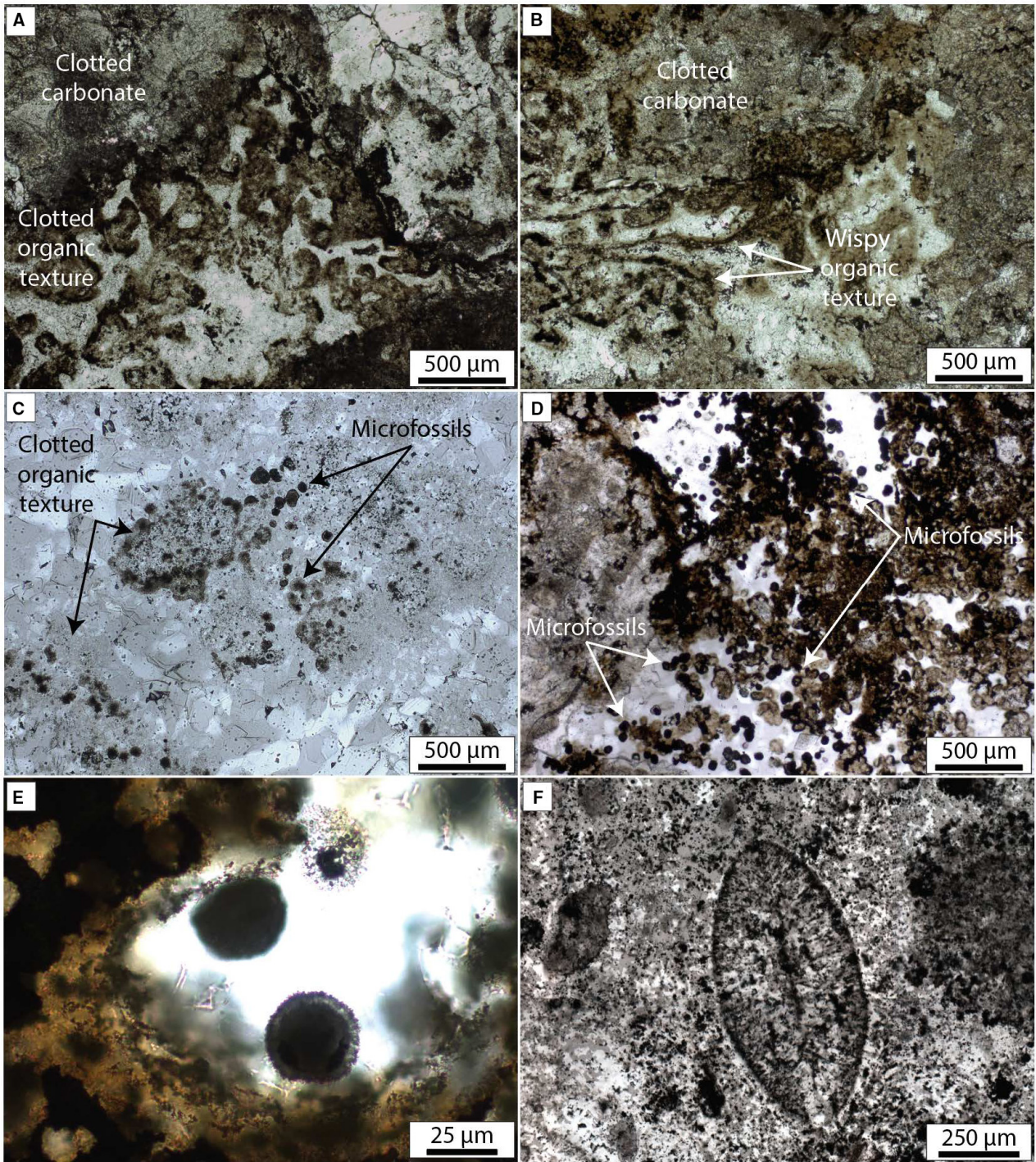
Fig. 9. Characteristic organic textures in chert-rich facies: (A) clotted organic textures; (B) wispy, diffuse, branching organic strands; (C) microclotted organic matter with light-toned mottling and microfossils; (D) various spherical microfossils morphotypes clustered in a clotted region of chert; (E) representative microfossil morphotype characterized by a dark, organic-rich wall, an organic-rich interior and a fringe; (F) coffee-bean like microfossil in a region of clotted carbonate.

Table 2. Fossil morphotypes present across the chert-rich facies in cores from wells A, B and C with representative images.
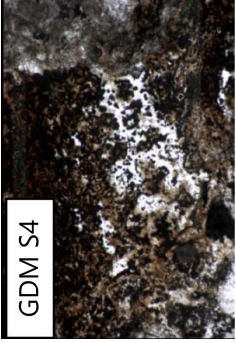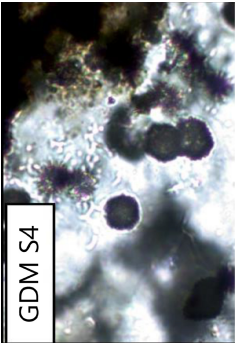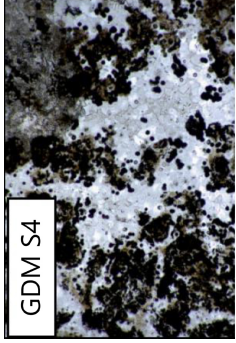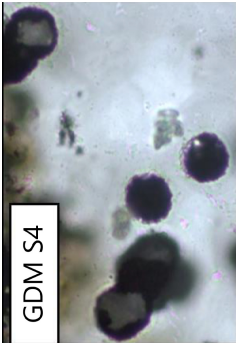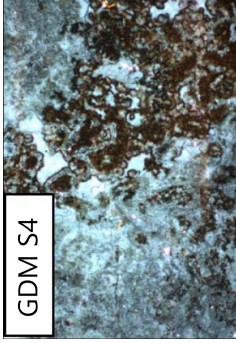
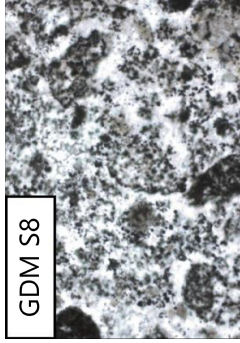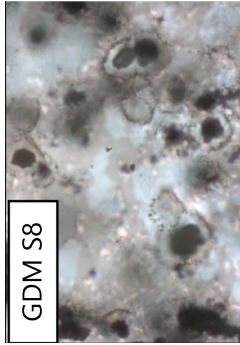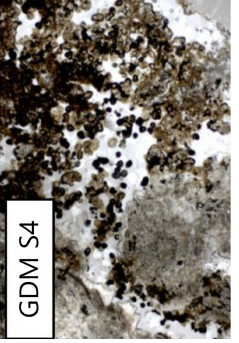| Morphotype	Description	Present in:	Wall?	Internal or surface structure?	10× magnification 200 µm	100× magnification 20 µm
1	*ca* 5–10 µm diameter organic walled spheres	GDM S4, GDM S8	Yes	None	GDM S4	GDM S4
2	*ca* 10–20 µm diameter organic walled spheres	GDM S4, GDM S8	Yes	None	GDM S4	GDM S4
3	Hollow *ca* 5–10 µm spheres with a <5 µm organic wall that drapes in *ca* 30–50 µm long chains over the carbonate grains	GDM S4	Yes	None	GDM S4	GDM S4
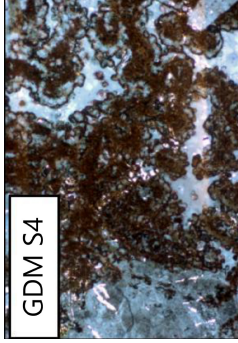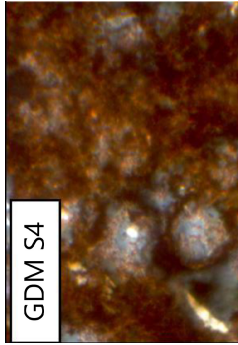
Table 2.   (continued)

Morphotype	Description	Present in:	Wall?	Internal or surface structure?	10× magnification 200 μm	100× magnification 20 μm
4	*ca* 10–15 μm diameter spheres with an organic-rich interior, thin outer organic wall, and chert fill between the wall and interior	GDM S8	Yes	None	GDM S8	GDM S8
5	*ca* 20–30 μm diameter organic walled spheres	GDM S4	Yes	Internal structures	GDM S4	GDM S4
6	*ca* 20–30 μm diameter spheres with a single <5 μm thick organic wall filled with microcrystalline chert	GDM S4	Yes	No	GDM S4	GDM S4
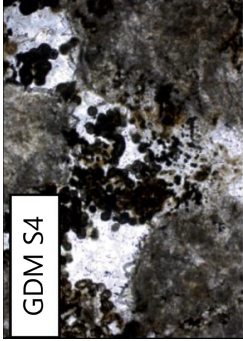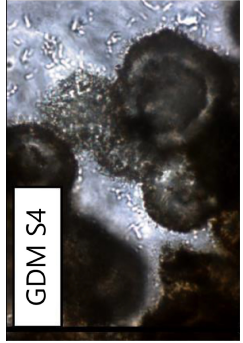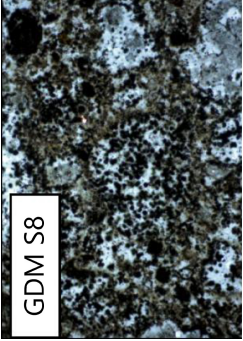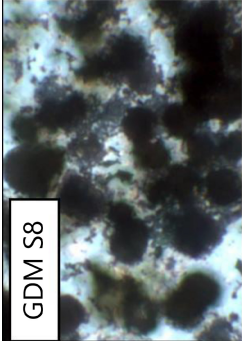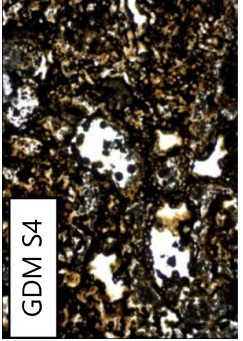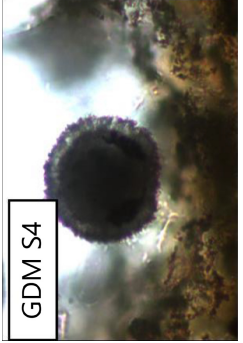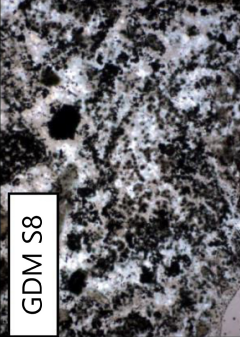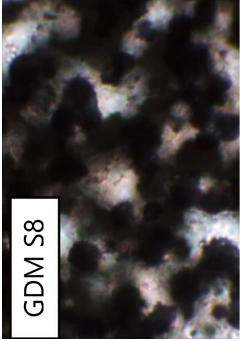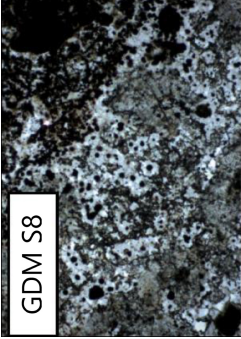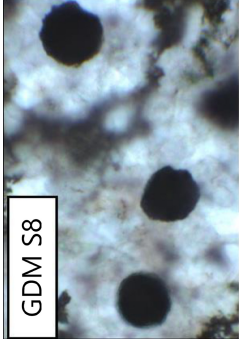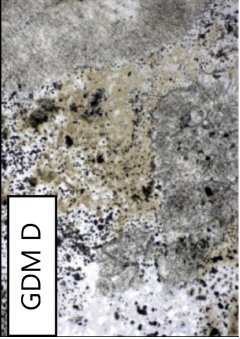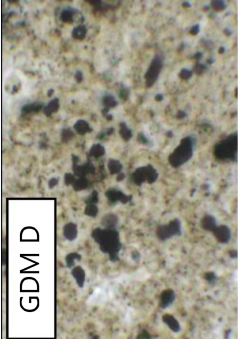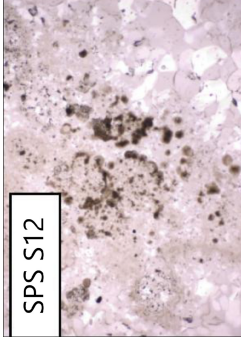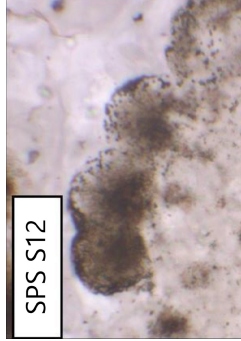
Table 2. (continued)

Morphotype	Description	Present in:	Wall?	Internal or surface structure?	10× magnification 200 μm	100× magnification 20 μm
7	*ca* 25–35 μm diameter spheres with two concentric organic rich walls, each <5 μm in diameter, filled with chert between walls and within the inner wall	GDM S4	Yes	Internal and surface features	GDM S4	GDM S4
8	*ca* 10–20 μm diameter spheres filled with organic material	GDM S4, GDM S8, SPS S19	No	None	GDM S8	GDM S8
9	*ca* 20–30 μm diameter spheres filled with organic material with a distinct outer wall and a tube-like fringe	GDM S4, SPS S12	No	Surface features	GDM S4	GDM S4

Table 2. (continued)

Morphotype	Description	Present in:	Wall?	Internal or surface structure?	10× magnification 200 µm	100× magnification 20 µm
10	*ca* 5–10 µm diameter spheres filled with organic material	GDM S8, GDM D	No	None	GDM S8	GDM S8
11	*ca* 20–30 µm diameter spheres, isolated within an envelope of chert	GDM S8	No	None	GDM S8	GDM S8
12	*ca* 5–10 µm diameter spheres with a 'silica envelope' or rim	GDM D, SPS S12	No	None	GDM D	GDM D
13	Spheroidal type structure comprised of many organic nanospheres	SPS S12	No	None	SPS S12	SPS S12
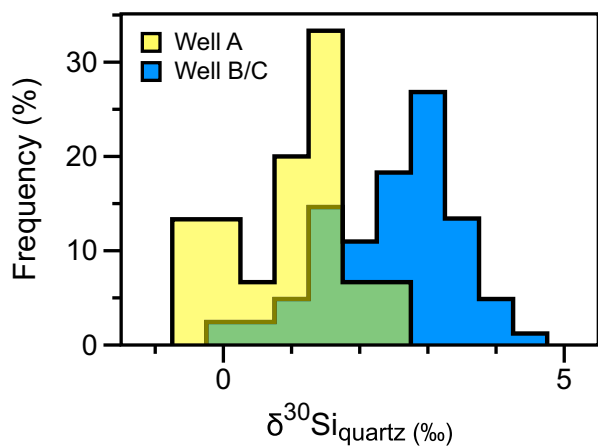
Fig. 10. Plot showing frequency of *in situ* δ^{30}Si values of early quartz for Well A ($n = 15$) and Well B ($n = 82$) samples. All data are between $-0.5‰$ and $4.5‰$, but samples from Well A (yellow) are generally lighter (average δ^{30}Si $= 1.0 \pm 0.8‰$), and samples from Well B and C (blue) are heavier (average δ^{30}Si $= 2.5 \pm 1.0‰$).

Fig. 11. Plot showing *in situ* δ^{18}O values of early chert. Upper panel shows variation in δ^{18}O for all data ($n = 157$). Lower panel shows temperature dependence of δ^{18}O quartz in equilibrium fixed δ^{18}O water values calculated using the oxygen isotope fractionation equation of Sharp *et al.* (2016). The shaded yellow and blue areas represent interquartile range for Well A ($n = 46$) and Well B and C ($n = 111$) samples, respectively.

Rather than cross-cutting the carbonate, an initial chert rim formed around the partially dissolved carbonate grains and was followed by at least one subsequent generation of silica and sometimes multiple generations (Figs 6 and 7), all of which likely precipitated rapidly from the same fluid.

Based on these observations, the authors propose that these samples collectively represent a microfossiliferous chert boundstone facies that contains one of the earliest generations of silica in the pre-salt deposits – a synsedimentary chert that preserved kerogen, delicate microbial structures, and microfossils. Through characterization of the chert-carbonate relationships, the formation mechanisms and depositional environments of both the chert and carbonate can be untangled. This may help to constrain the silica paragenesis, water chemistry and water sources, and provide a window into the biosphere in the ancient basin.

Decoupled chert and carbonate precipitation and implications

The dominant chemical sediments in the BVF and other pre-salt deposits contain carbonates, Mg-silicates and late diagenetic silica phases, but they typically lack authigenic chert. This indicates that authigenic or synsedimentary chert did not precipitate alongside carbonates in the majority of the basin. Previous studies have suggested that these

facies formed in an alkaline lake in which Mg-silicate clays were the dominant silica sink (Wright, 2012; Wright & Barnett, 2015, 2017; Wright & Tosca, 2016; Pietzsch *et al.*, 2018, 2020; Tosca & Wright, 2015; Tutolo & Tosca, 2018; Carramal *et al.*, 2022). This is consistent with models and experimental studies that have shown that Mg-silicates are the dominant silica phase that precipitates from alkaline fluids at elevated pH (Tosca *et al.*, 2011; Strauss & Tosca, 2020; Chase *et al.*, 2021). However, the rare chert–boundstone facies likely formed under a different set of conditions compared to carbonates and Mg-silicate clays.

The carbonate and chert in the chert–boundstone facies each display features consistent with primary precipitation, suggesting that both formed as authigenic phases. However, the textures, chemistry, and boundary relationships of these phases suggest that they did not form

contemporaneously. The presence of angular to rounded, transported intraclasts as well as dissolution textures (including etched margins of clasts, solution-enlarged pores, and erosion surfaces) across all carbonate fabrics in the chert-rich samples suggest that the carbonate experienced periods of dissolution and alteration after forming. These textures, the sharp boundaries between the microcrystalline chert and carbonate, the organic encrustation of the carbonate, and the carbonate-rimming chert that overgrows rather than cross-cuts carbonate and shows multiple generations of growth (Figs 6 and 7) all suggest that chert precipitation post-dated both the formation and the subsequent dissolution/alteration of the carbonate. Thus, although both phases likely formed as primary precipitates, they precipitated at different times with the carbonate being the earliest precipitate.

The genetic history of chert and carbonate precipitation in the BVF is striking and differs from classic examples of early diagenetic chert and carbonate deposits. The best examples of early formed chert and carbonate within a single formation come from Proterozoic marine deposits (Sergeev & Sharma, 2012; Butterfield, 2015; Demoulin *et al.*, 2019; Moore *et al.*, 2023, and references therein). These were widespread during the Proterozoic in large part because the absence of silicifying organisms allowed for higher concentrations of silica in aqueous environments and early silica precipitation (Maliva *et al.*, 1989, 2005; Siever, 1992). The evolution of biosilicification in the Phanerozoic significantly depleted silica in the ocean and other aqueous environments, making the precipitation of silica alongside carbonate far less common (Maliva *et al.*, 1989, 2005; Siever, 1992). The BVF is a rare example of a Phanerozoic deposit that contains both syndepositional chert and carbonate. Like Proterozoic marine tidal deposits, carbonate dominates the BVF with only rare occurrences of authigenic chert. However, the temporal decoupling of the carbonate and chert in the BVF is different from Proterozoic deposits where carbonate and chert formed under similar conditions in the same environment. In addition to being temporally decoupled, the chert likely formed from a fluid that was chemically distinct from the largely alkaline water body that promoted the precipitation of carbonate. Studies have shown that Mg-silicate precipitation typically occurs at high pH (Tosca *et al.*, 2011; Strauss & Tosca, 2020; Chase *et al.*, 2021). Unlike carbonate and Mg-silicate clay precipitation, amorphous silica polymerization at surface temperatures generally requires lower pH fluids and the silica concentrations must be high enough to reach silica saturation (Krauskopf, 1956; Iler, 1979). This suggests that the chert and Mg-silicate clays formed from different fluids with distinct pH and fluid chemistry. Thus, a new model is required to explain both the chert-carbonate paragenesis and the precipitation of synsedimentary, authigenic chert within the pre-salt basin.

Silica precipitation on a karsted landscape

Data presented here suggest that the chert boundstone facies accumulated in a karstified carbonate terrain (e.g. Wright, 2012) that was cemented at the surface by primary silica. The poorly sorted, angular to subangular carbonate clasts visible at core scale (*ca* 2 cm to 20 cm) and in thin section (*ca* 10 μm to 1 mm) are characteristic of karst breccias (Kerans, 1988, 1993; Loucks, 1999; Wang & Al-Aasm, 2002; Liu & Jiang, 2018; Fu, 2019) and are found alongside mosaic fracturing (Loucks, 1999). The dissolution features and recrystallization textures – mottled textures, patchy dissolution of carbonates, and corroded surfaces of the clotted and shrub-like carbonate – are further evidence of karstification (Dickson & Saller, 1995; Weidlich, 2010; Liu & Jiang, 2018). Cores of the BVF reveal that rocks with these textures are capped by truncation surfaces suggesting that millimetre to centimetre-scale secondary porosity is genetically linked to an intraformational exposure surface. Together, these observations suggest that the shrub-like and clotted carbonate structures precipitated from the alkaline lake water and subsequently experienced a period of dissolution and karstification. This was likely related to a drop in lake level and dissolution of carbonate due to introduction of a new fluid. It is possible that the fluid that drove carbonate dissolution and the fluid from which silica precipitated were the same, resulting in penecontemporaneous dissolution of carbonate and precipitation of chert.

The localized formation of primary chert may have been driven by spatially restricted pulses of a silica-rich fluid into the basin after the formation and karstification of the carbonate. Two potential sources could explain the precipitation of chert. The first is a silica-rich hydrothermal source (scenario 1). In modern hot springs, as the silica-rich fluid moves away from the source and cools, it becomes supersaturated with respect to amorphous silica, resulting in rapid precipitation of silica that encases microbial communities and organic

matter in the vicinity (Walter *et al.*, 1972; Ferris *et al.*, 1986; Schultze-Lam *et al.*, 1995; Jones & Renaut, 1996; Konhauser & Ferris, 1996; Jones *et al.*, 1997, 1998a; Konhauser & Urrutia, 1999; Konhauser *et al.*, 2001; Campbell *et al.*, 2002, 2015; Cady & Farmer, 2007). This type of silicification is also found in the rock record in formations like the Rhynie Chert (in Scotland), a fossiliferous Devonian sinter deposit (Rice *et al.*, 2002; Edwards *et al.*, 2018; Garwood *et al.*, 2019; Strullu-Derrien *et al.*, 2019). The mixing of the lake water with a localized source of low pH, silica-rich fluid, or the introduction of this fluid during a period of subaerial exposure would have created microenvironments in the basin that were chemically distinct from the alkaline lake and may have favoured silica polymerization over carbonate and Mg-silicate clay precipitation.

Alternatively, low temperature, silica-rich freshwaters introduced into the basin via surface runoff or groundwater percolation could explain the localized precipitation of silica (scenario 2). The introduction of a freshwater fluid into a karst terrain – either from rivers or from groundwater percolation through springs in an exposed lake rim or island – would have created a microenvironment characterized by lower pH and alkalinity than the surrounding lake water. Although silica precipitation from these freshwater sources is not typically observed in modern environments, the absence or sparsity of biosilicifying organisms in terrestrial or lacustrine environments during the Cretaceous (Sims *et al.*, 2006; Knoll & Follows, 2016; Conley *et al.*, 2017) may have allowed rivers or groundwater that flowed through mafic or felsic bedrock to contain elevated concentrations of silica. Even if concentrations were not above 120 ppm in the source fluid, evaporation of silica-rich river water or groundwater in a subaerially-exposed karst terrain may have further concentrated silica to promote localized, rapid silica precipitation.

Measured $\delta^{30}Si$ values ranging from -0.5‰ to 4.5‰ (Fig. 10) are inconsistent with hydrothermal precipitation which predicts lighter silicon isotope compositions, with $\delta^{30}Si$ values typically below 2‰ (Van Den Boorn *et al.*, 2010; Kleine *et al.*, 2018). In contrast, studies of the $\delta^{30}Si$ of meteoric water (De La Rocha *et al.*, 2000; Ding *et al.*, 2004; Georg *et al.*, 2006) and Proterozoic cherts (Chakrabarti *et al.*, 2012; Marin-Carbonne *et al.*, 2014, and references therein) show elevated values relative to continental crust and basalt (which typically range between -1‰ and 1‰;

Opfergelt & Delmelle, 2012). This is largely because formation of authigenic silicate clays and soil-forming processes in rivers preferentially incorporates ^{28}Si. As a result, the fluid becomes progressively enriched in ^{30}Si (De La Rocha *et al.*, 2000; Ding *et al.*, 2004; Georg *et al.*, 2006; Chakrabarti *et al.*, 2012; Marin-Carbonne *et al.*, 2014, and references therein). In a system with elevated concentrations of silica that saw chert precipitation as the final sink, the chert may similarly be enriched in ^{30}Si. A hydrothermal origin for this chert facies is also inconsistent with the observed $\delta^{18}O$ values, averaging at 34.6 ± 2.1‰ for Well A and 36.9 ± 1.8‰ for Wells B and C. Calculations using end member $\delta^{18}O$ values of water sourced either from the lake fluid (highest $\delta^{18}O$ values) or from rain water (lowest $\delta^{18}O$ values) suggest that the chert formed at temperatures between 8°C and 54°C (Fig. 11). Even the most conservative of these temperatures are low compared to most hydrothermal systems, and the more realistic estimates – which assume chert formation from a fluid that was distinct from the lake water – are more consistent with formation at temperatures below 54°C. Thus, both the $\delta^{30}Si$ and the $\delta^{18}O$ values of the chert are more consistent with silica precipitation from a low temperature groundwater or river water source. It is worth noting that there is significant spread in the $\delta^{30}Si$, which could point to nuanced complexity in the silica sources. If these silica-precipitating microenvironments experienced mixing of freshwater with the lake water, some of the silica may have been sourced from the lake fluid through dissolution of Mg-silicate clays. Such a mixing scenario could result in variability in $\delta^{30}Si$ of the chert. Although the lake may have been similarly fed by rivers and groundwater, the evolution of the basin as a whole and evaporitic processes would have resulted in a more evolved fluid with a composition that was chemically distinct from that of the rivers or groundwater.

Organic matter and taphonomic windows

In addition to forming from different fluids at different times, the chert and carbonate facies represent distinct taphonomic windows. The organic matter preserved in primary chert is both texturally and compositionally different from the organic matter in the carbonate facies and points to different taphonomic histories. The organic matter in the carbonate facies is spatially correlated with secondary porosity, displays sharp contacts with the surrounding carbonate, and is

associated with late diagenetic quartz and carbonate crystals, all of which are characteristic features of remobilized bitumen (Mastalerz *et al.*, 2018; Wood *et al.*, 2018; Misch *et al.*, 2019). Thus, the carbonate-associated organic matter is interpreted as bitumen that formed from thermal alteration of kerogen at the onset of the oil window and filled void spaces in the carbonates. In contrast, the fluffy, diffuse texture of the organic matter preserved within the chert matrix of chert–boundstones more closely resembles primary kerogen typically described in association with Proterozoic microfossils preserved in early diagenetic or primary chert (e.g. Schopf, 1992; Sergeev & Sharma, 2012; Butterfield, 2015; Demoulin *et al.*, 2019; Moore *et al.*, 2023, and references therein). Furthermore, the lower O/C ratio of the organic matter in carbonate facies compared to organic matter preserved by primary chert suggests that the latter is less thermally mature based on the inverse relationship observed between O/C ratio and progressive alteration (Tissot & Welte, 1984; Hunt *et al.*, 2002; Vandenbroucke, 2003). Based on the above petrographic and geochemical observations, the organic matter preserved in chert–boundstone facies is consistent with primary organic matter rather than thermally mature bitumen found elsewhere in the pre-salt deposits.

Despite hypotheses that carbonate shrubs may have formed through biogenic processes (Terra *et al.*, 2009; Chafetz *et al.*, 2018), the earliest formed minerals in the Barra Velha Formation (chert and carbonate) consistently demonstrate that chert preserves primary organic matter while carbonate does not. The type and distribution of organic matter preserved throughout the Barra Velha Formation is noteworthy because it suggests either: (i) primary differences in the distribution of biota in the lake; or (ii) taphonomic differences. Respectively, then, either: (i) the carbonate precipitating environments were not habitable and therefore formed in the absence of organic material while the chert precipitating environments were inhabited; or (ii) the environmental conditions or mechanisms of carbonate formation were not conducive to the preservation of organic material while the conditions and mechanisms that characterized chert formation were.

The high alkalinity of the fluid from which carbonates and Mg-silicate clays formed made it a somewhat extreme environment (Wright, 2012; Wright & Barnett, 2015; Wright & Tosca, 2016; Pietzsch *et al.*, 2018, 2020; Tosca & Wright, 2015;

Tutolo & Tosca, 2018; Mercedes-Martín *et al.*, 2019; Carramal *et al.*, 2022). This is evidenced by the dominance of ostracod fossils and few other macroscopic fossils throughout many previously studied pre-salt deposits (Pietzsch *et al.*, 2018). However, many known microbial organisms (bacteria, archaea, and simple eukaryotes) are adapted to thrive in or tolerate alkaline environments (Jones *et al.*, 1998a, 1998b; Jones & Grant, 2000; Roadcap *et al.*, 2006; Pikuta *et al.*, 2007). Similar microorganisms may have inhabited the proto-Atlantic basin. This is supported by biomarker analysis of the BVF, which identifies the presence of halo-tolerant algal species and anaerobic organisms commonly found in saline-stratified lakes (Mello *et al.*, 2021). Given that these organisms can thrive even in extreme end members of alkalinity, pH, and temperature, it is unlikely that the absence of primary organic material in carbonate from the BVF is the result of the carbonate and Mg-clay precipitating environments being uninhabited. Studies of modern alkaline lakes have found that, although these environments tend to be highly productive, the organic matter is rapidly remineralized and little is buried and preserved (Haines *et al.*, 2023). A similar rapid remineralization process in the alkaline lake fluid of the pre-salt basin may explain the absence of organic microfossils in the carbonates. The authors therefore conclude that the differences in primary organic matter and distribution of potential microfossils across different facies is the result of taphonomic differences between the chert and carbonate precipitating environments.

Pre-salt microbiota

The preservation of primary organic matter and potential microfossils in the chert–boundstone facies defines a rare taphonomic window into the ecology of the pre-salt basin. The wispy organic lamination in some samples is reminiscent of biofilms and the clotted organic microfabrics are similar to clotted microfabrics associated with microbialites (Riding, 1991, 2000; Shapiro, 2000), suggesting that benthic microbial communities inhabited these chert-precipitating environments. The encrustation of carbonate grains and fabrics by organic matter in some samples and the microboring are further evidence of benthic communities. Together, these fabrics point to colonization of the karst environment, either introduced by the surface water or groundwater fluids, or representing a

distinct biota adapted to a partially exposed and evaporitic environment. In addition to the textures present in both chert and carbonate in the chert–boundstone facies, the organic structures with diverse morphologies may represent a range of microfossils of bacteria, simple eukaryotes, and possibly pollen.

Different potential fossil morphotypes are preserved alongside one another within any given sample. This suggests that differences in morphology do not reflect taphonomic differences acting upon the same structures but rather reflect diversity in the original structures. The walled structures (categories A and B) closely resemble the classic fossilization style of microfossils in chert which are typically characterized by preservation of an organic wall thought to be remnant sheaths or cell envelopes (e.g. Schopf, 1992; Sergeev & Sharma, 2012; Butterfield, 2015; Demoulin *et al.*, 2019; Moore *et al.*, 2023, and references therein). The smaller organic walled structures have size ranges most consistent with bacterial cells (e.g. Koch & Ehrenfeld, 1968; Demoulin *et al.*, 2019, and references therein), although the simple nature of the spheres precludes further classification. The larger organic walled structures, on the other hand, sometimes have complex internal structures (for example, Types 3 and 7; Table 2) and size ranges that are more consistent with simple eukaryotes (Knoll, 2014). These structures may be fossils of eukaryotic algae, such as unicellular chlorophyte algae (Domozych *et al.*, 2016; Samolov *et al.*, 2020), though they are also quite simple and may represent a range of other single-celled eukaryotes (e.g. Knoll, 2014).

The category C structures are unique in the amount of organic material preserved and the lack of a distinct envelope. One possible explanation is that these structures represent droplets of oil that were released by the underlying source rocks into the silica-rich fluid and preserved in the chert. This would explain why they are organic throughout rather than preserved as hollow, organic-walled spheres. However, the uniformly high O/C ratio of organic matter across the range of morphotypes (organic walled structures and dense organic spheres) and the clear distinction between the O/C ratio of organic matter in chert–boundstone facies and bitumen that fills voids in the surrounding carbonate facies argue against this interpretation. Furthermore, the larger scale textures of organic material throughout these samples, which resemble a range of benthic microbial textures

(encrustation, clotted microfabrics, and crinkly microbial lamination), indicate that this environment was colonized by microbial communities and experienced rapid silica precipitation. Therefore, the composition and context of the organic material in these structures are consistent with an interpretation that category C structures also represent microfossils.

The unique preservation of category C structures alongside hollow-walled microfossils may have been the result of physiological or biochemical differences across different organisms that inhabited this environment. The dense spheres (Table 2) have sizes which could be consistent with either bacteria (e.g. Koch & Ehrenfeld, 1968; Demoulin *et al.*, 2019, and references therein) or eukaryotes (Knoll, 2014). One possibility is that these structures represent eukaryotic algae or algal spores whose physiology allowed for a greater degree of organic preservation than the organic-walled structures. Modern examples of highly recalcitrant algae include various types of Chlorophyte algae, some of which produce sporopollenin, an especially resistant polymer that coats the surfaces of cells (Brooks & Shaw, 1978; Komaristaya & Gorbulin, 2006). These structures also resemble various fossils interpreted as unicellular algae. For example, the tube-like surface fringe features of some structures (for example, Type 5 in GDM S4 and Type 1 in SPS S12) resemble Chlorophyte algal fossils preserved by phosphate in the Dengying Formation in China (Chai *et al.*, 2022) and by chert in the Rhynie Chert (Strullu-Derrien *et al.*, 2021). The fossil Chlorophyte algae preserved in the Rhynie Chert also contain organic material in the microfossil interior (Edwards & Lyon, 1983) like the structures described here. Another possibility is that these structures are especially recalcitrant structures like small pollen grains, fungal spores or plant spores which may also be coated in sporopollenin (Li *et al.*, 2018). Fossil plant spores are preserved in the Rhynie Chert and have a dense organic appearance and occasional internal structure and surface ornamentation preserved (Cascales-Miñana *et al.*, 2022) similar to some of the structures preserved in chert in the BVF.

The category D structures are also unique and differ from classical microfossil morphologies. Rather than either the organic walls or dense organic spheres, these structures are packages of organic nanospheres that individually are much smaller than eukaryotic organisms and most bacteria. Two modern organisms have a similar appearance to these structures. One is a type of colonial cyanobacteria – *Coelosphaerium* – that

form packages of cells *ca* 9 to 23 µm in diameter that contain individual cyanobacterial cells *ca* 2 to 3 µm in diameter (Godo *et al.*, 2017). The other is a single-celled, spherical, eukaryotic Volvocacean algae which is characterized by clusters of individual algal cells or larger cells that contain nanoscopic differentiated somatic cells (Hallmann, 2006; Coleman, 2012) similar to category D structures. Whether bacterial or eukaryotic, these structures represent a morphotype that is distinct from the category A to C structures and demonstrate further microbial diversity.

Interestingly, plant fossils and most other complex eukaryotes seem to be conspicuously absent in the BVF. The exception are the rare category E 'coffee bean' structures, which are likely ostracod fossils and closely resemble previously described ostracod fossils present in other pre-salt deposits (e.g. Vázquez-García *et al.*, 2021). If plants or other complex eukaryotes (aside from ostracods) did inhabit any microenvironments in the lake, the processes that facilitated chert formation would have likely preserved them similarly to the preservation of a range of organisms seen in the Rhynie Chert (Rice *et al.*, 2002; Strullu-Derrien *et al.*, 2019). The absence of these types of fossils in the chert boundstones or other facies suggests that harsh conditions persisted in most environments in the lake throughout its evolution. The presence of ostracods further supports an interpretation of persisting harsh conditions in the basin. Despite these potentially harsh conditions, however, the chert–boundstone facies demonstrate that a range of microorganisms (bacterial and eukaryotic with potential algae and fungi) thrived in at least some parts of the basin throughout its evolution.

CONCLUSIONS

Chert-rich facies in the Brazilian margin of the pre-salt basin provide new insights into the complexity and evolution of the basin and the microbial communities that inhabited it. The textures, composition, grain/matrix boundary relationships, and the lack of cross-cutting relationships between the chert and carbonate in these rocks suggest that both carbonate and chert formed via primary chemical precipitation before burial and compaction. However, their formation was temporally decoupled. The authors suggest that these fossiliferous chert-rich facies formed after subaerial exposure and karstification of the primary carbonates that precipitated within the

alkaline lake. The textures and composition of the chert suggest that it formed from a fluid distinct from the alkaline lake water which was later introduced after karstification of the carbonates. This fluid was likely sourced from rivers or groundwater and was characterized by neutral pH, low temperatures, and elevated silica concentrations. This later fluid allowed for a change in chemical conditions in microenvironments which promoted the formation of chert rather than carbonates and Mg-silicate clays. Together, these observations reveal that the pre-salt basin saw complex localized changes in water chemistry throughout its history as a result of changing lake level and the introduction of chemically diverse fluids. Through characterization of these complexities and the chemistry of different fluid sources and their relationships to lake level fluctuations, a more complete understanding of the history and evolution of the basin leading up to the marine incursion recorded by the overlying evaporite succession can be formed.

The preservation of primary organic material and microfossils in the chert provide evidence that a diverse microbiota thrived in at least some microenvironments in the basin. The microbes and simple eukaryotes preserved by chert may represent communities already present in the lake, communities that colonized the karst terrain, communities introduced by the terrestrial source fluids, or some combination of these. Additionally, the notable absence of complex eukaryotic fossils aside from ostracods in the fossiliferous chert–boundstone facies point to persisting harsh conditions of the basin. The notable difference in preservation of organic material between chert and carbonate facies and the reasons for this difference (related to taphonomy or habitability) remains a mystery. However, based on the presence of microbes in at least some microenvironments and the similarities in clotted microfabrics in both chert and carbonate, the authors suggest that the preferential preservation of primary organic material in chert rather than carbonate reflects taphonomic differences rather than differences in habitability of carbonate and chert precipitating environments. Further work is required to characterize the reasons and mechanisms that underpin these taphonomic differences.

project. We also thank Y. Guan for operating the Secondary Ion Mass Spectrometer and discussions regarding data postprocessing and analytical artefacts. Additional thanks to E. Adams, R. Newport, L. Fadel Cury, A. Bahniuk and H. Albrecht for helpful conversations, and two reviewers for their insightful comments and suggestions. Additional thanks to D. Hutkin for support.

DATA AVAILABILITY STATEMENT

All data supporting the findings of this work are provided in the figures, tables, and supplemental files of the work.

REFERENCES

Azerêdo, A.C., **Duarte, L.V.** and **Silva, A.P.** (2021) The challenging carbonates from the Pre-Salt reservoirs offshore Brazil: facies, palaeoenvironment and diagenesis. *J. South Am. Earth Sci.*, **108**, 103202.

Barnett, A.J., **Obermaier, M.**, **Amthor, J.**, **Sharafodin, M.**, **Bolton, M.**, **Clarke, D.** and **Camara, R.** (2018) *Origin and significance of thick carbonate grainstone packages in non-marine successions: a case study from the Barra Velha Formation, Santos Basin*, pp. 20–23. AAPG Special Volumes, Salt Lake City, UT.

Barnett, A.J., **Obermaier, M.**, **Amthor, J.**, **Sharafodin, M.**, **Bolton, M.**, **Clarke, D.** and **Camara, R.** (2021) Chapter 6: Origin and significance of thick carbonate grainstone packages in nonmarine successions: A case study from the Barra Velha Formation, Santos Basin, Brazil. In: *Memoir 124: The Supergiant Lower Cretaceous Pre-Salt Petroleum Systems of the Santos Basin, Brazil* (Eds Mello, M.R., Yilmaz, P.O. and Katz, B.J.), pp. 155–174. AAPG. https://doi.org/10.1306/13722318MSB.6.1853.

Bastos, L.P.H., **Jagniecki, E.A.**, **Holanda dos Santos, W.**, **da Costa Cavalcante, D.**, **Jorge de Menezes, C.**, **Ferreira Alferes, C.L.**, **Neves da Silva, D.B.**, **Bergamaschi, S.**, **Rodrigues, R.** and **Pereira, E.** (2022) Organic geochemical evidence for the transition of Aptian-Albian hypersaline environments into marine restricted seas: The South Atlantic oceanic northern gateway and its implications for the pre-salt deposits. *Marine Petrol. Geol.*, **140**, 105632.

Bowen, G.J. and **Wilkinson, B.** (2002) Spatial distribution of δ18O in meteoric precipitation. *Geology*, **30**, 315–318.

Brooks, J. and **Shaw, G.** (1978) Sporopollenin: A review of its chemistry, palaeochemistry and geochemistry. *Grana*, **17**, 91–97.

Butterfield, N.J. (2015) Proterozoic photosynthesis – a critical review. *Palaeontology*, **58**, 953–972.

Cady, S.L. and **Farmer, J.D.** (2007) Fossilization processes in siliceous thermal springs: Trends in preservation along thermal gradients. In: *Novartis Foundation Symposia* (Eds Bock, G.R. and Goode, J.A.), pp. 150–173. John Wiley & Sons, Ltd., Chichester.

Campbell, K.A., **Rodgers, K.A.**, **Brotheridge, J.M.A.** and **Browne, P.R.L.** (2002) An unusual modern silica–carbonate sinter from Pavlova spring, Ngatamariki, New Zealand. *Sedimentology*, **49**, 835–854.

Campbell, K.A., **Lynne, B.Y.**, **Handley, K.M.**, **Jordan, S.**, **Farmer, J.D.**, **Guido, D.M.**, **Foucher, F.**, **Turner, S.** and **Perry, R.S.** (2015) Tracing biosignature preservation of geothermally silicified microbial textures into the geological record. *Astrobiology*, **15**, 858–882.

Carminatti, M., **Wolff, B.** and **Gamboa, L.** (2008) New exploratory frontiers in Brazil. In: *19th World Petroleum Council, Energy Institute (Great Britain)*, p. 19. Energy Institute, Madrid.

Carramal, N.G., **Oliveira, D.M.**, **Cacela, A.S.M.**, **Cuglieri, M.A.A.**, **Rocha, N.P.**, **Viana, S.M.**, **Toledo, S.L.V.**, **Pedrinha, S.** and **de Ros, L.F.** (2022) Paleoenvironmental insights from the deposition and diagenesis of Aptian pre-salt magnesium silicates from the Lula Field, Santos Basin, Brazil. *J. Sediment. Res.*, **92**, 12–31.

Cascales-Miñana, B., **Servais, T.**, **Capel, E.** and **Steemans, P.** (2022) Further observations on the spores of the Rhynie chert plant Horneophyton lignieri (Kidston & Lang) Barghoorn & Darrah, 1938: Implications for palaeodiversity studies. *Rev. Palaeobot. Palynol.*, **296**, 104543.

Chafetz, H., **Barth, J.**, **Cook, M.**, **Guo, X.** and **Zhou, J.** (2018) Origins of carbonate spherulites: Implications for Brazilian Aptian pre-salt reservoir. *Sediment. Geol.*, **365**, 21–33.

Chai, S., **Aria, C.** and **Hua, H.** (2022) A stem group Codium alga from the latest Ediacaran of South China provides taxonomic insight into the early diversification of the plant kingdom. *BMC Biol.*, **20**, 1–10.

Chakrabarti, R., **Knoll, A.H.**, **Jacobsen, S.B.** and **Fischer, W.W.** (2012) Si isotope variability in Proterozoic cherts. *Geochim. Cosmochim.*, **91**, 187–201.

Chase, J.E., **Arizaleta, M.L.** and **Tutolo, B.M.** (2021) A series of data-driven hypotheses for inferring biogeochemical conditions in alkaline lakes and their deposits based on the behavior of Mg and SiO_2. *Minerals*, **11**, 106–125.

Coleman, A.W. (2012) A comparative analysis of the Volvocaceae (Chlorophyta). *J. Phycol.*, **48**, 491–513.

Conley, D.J., **Frings, P.J.**, **Fontorbe, G.**, **Clymans, W.**, **Stadmark, J.**, **Hendry, K.R.**, **Marron, A.O.** and **De La Rocha, C.L.** (2017) Biosilicification drives a decline of dissolved Si in the oceans through geologic time. *Front. Mar. Sci.*, **4**, 1–19.

De La Rocha, C.L., **Brzezinski, M.A.** and **DeNiro, M.J.** (2000) A first look at the distribution of the stable isotopes of silicon in natural waters. *Geochim. Cosmochim.*, **64**, 2467–2477.

Demoulin, C.F., **Lara, Y.J.**, **Cornet, L.**, **François, C.**, **Baurain, D.**, **Wilmotte, A.** and **Javaux, E.J.** (2019) Cyanobacteria evolution: Insight from the fossil record. *Free Radic. Biol. Med.*, **140**, 206–223.

Dickson, J.A.D. and **Saller, A.H.** (1995) Identification of Subaerial Exposure Surfaces and Porosity Preservation in Pennsylvanian and Lower Permian Shelf Limestones, Eastern Central Basin Platform, Texas. In: *Unconformities and Porosity in Carbonate Strata* (Eds Budd, D.A., Saller, A.H. and Harris, P.M.), *American Association of Petroleum Geologists*, **63**, 239–257.

Ding, T., **Wan, D.**, **Wang, C.** and **Zhang, F.** (2004) Silicon isotope compositions of dissolved silicon and suspended matter in the Yangtze River, China. *Geochim. Cosmochim.*, **68**, 205–216.

Domozych, D.S., **Popper, Z.A.** and **Sørensen, I.** (2016) Charophytes: Evolutionary giants and emerging model organisms. *Front. Plant Sci.*, **7**, 1–8.

Edwards, D.S. and **Lyon, A.G.** (1983) Algae from the Rhynie Chert. *Botanical J. Linnean Soc.*, **86**, 37–55.

Edwards, D., **Kenrick, P.** and **Dolan, L.** (2018) History and contemporary significance of the Rhynie cherts—our earliest preserved terrestrial ecosystem. *Philos. Trans. R Soc. BPhil. Trans. R Soc. B*, **373**, 1–7.

Ferris, F.G., **Beveridge, T.J.** and **Fyfe, W.S.** (1986) Iron-silica crystallite nucleation by bacteria in a geothermal sediment. *Nature*, **320**, 609–611.

Fu, Q. (2019) Characterization and discrimination of paleokarst breccias and pseudobreccias in carbonate rocks: Insight from Ordovician strata in the northern Tarim Basin, China. *Sedimentary Geol.*, **382**, 61–74.

Garwood, R.J., **Oliver, H.** and **Spencer, A.R.T.** (2019) An introduction to the Rhynie chert. *Geol. Mag.*, **157**, 47–64.

Georg, R.B., **Reynolds, B.C.**, **Frank, M.** and **Halliday, A.N.** (2006) Mechanisms controlling the silicon isotopic compositions of river waters. *Earth Planet. Sci. Lett.*, **249**, 290–306.

Godo, T., **Saki, Y.**, **Nojiri, Y.**, **Tsujitani, M.**, **Sugahara, S.**, **Hayashi, S.**, **Kamiya, H.**, **Ohtani, S.** and **Seike, Y.** (2017) Geosmin-producing species of coelosphaerium (Synechococcales, Cyanobacteria) in Lake Shinji, Japan. *Sci. Rep.*, **7**, 1–10.

Haines, M., **Khot, V.** and **Strous, M.** (2023) The vigor, futility, and application of microbial element cycles in alkaline Soda Lakes. *Elements*, **19**, 30–36.

Hallmann, A. (2006) Morphogenesis in the family volvocaceae: Different tactics for turning an embryo right-side out. *Protist*, **157**, 445–461.

Hunt, J.M., **Philp, R.P.** and **Kvenvolden, K.A.** (2002) Early developments in petroleum geochemistry. *Org. Geochem.*, **33**, 1025–1052.

Iler, K.R. (1979) *The chemistry of silica: solubility, polymerization, colloid and surface properties and biochemistry of silica*. John Wiley and Sons Ltd., New York.

Jones, B.E. and **Grant, W.D.** (2000) Microbial diversity and ecology of alkaline environments. In: *Journey to Diverse Microbial Worlds: Adaptation to Exotic Environments* (Ed Seckbach, J.), pp. 177–190. Springer, Dordrecht.

Jones, B. and **Renaut, R.W.** (1996) Influence of thermophilic bacteria on calcite and silica precipitation in hot springs with water temperatures above 90 °C: evidence from Kenya and New Zealand. *Can. J. Earth Sci.*, **33**, 72–83.

Jones, B., **Renaut, R.W.** and **Rosen, M.R.** (1997) Biogenicity of silica precipitation around geysers and hot-spring vents, North Island, New Zealand. *J. Sediment. Res.*, **67**, 88–104.

Jones, B., **Renaut, R.W.** and **Rosen, M.R.** (1998a) Microbial biofacies in hot-spring sinters; a model based on Ohaaki Pool, North Island, New Zealand. *J. Sediment. Res.*, **68**, 413–434.

Jones, B.E., **Grant, W.D.**, **Duckworth, A.W.** and **Owenson, G.G.** (1998b) Microbial diversity of soda lakes. *Extremophiles*, **2**, 191–200.

Kerans, C. (1988) Karst-controlled reservoir heterogeneity in Ellenburger Group carbonates of West Texas. *AAPG Bulletin*, **72**(10), 1160–1183.

Kerans, C. (1993) Description and Interpretation of Karst-Related Breccia Fabrics, Ellenburger Group, West Texas. In: *Arbuckle Group core workshop and field trip: Oklahoma Geological Survey* (Ed Johnson, K. S.), Special Publication 91–3, (pp. 145–156).

Kleine, B.I., **Stefánsson, A.**, **Halldórsson, S.A.**, **Whitehouse, M.J.** and **Jónasson, K.** (2018) Silicon and oxygen isotopes unravel quartz formation processes in the Icelandic crust. *Geochem. Persp. Let.*, **7**, 5–11.

Knoll, A.H. (2014) Paleobiological perspectives on early eukaryotic evolution. *Cold Spring Harb. Perspect. Biol.*, **6**, 1–14.

Knoll, A.H. and **Follows, M.J.** (2016) A bottom-up perspective on ecosystem change in Mesozoic oceans. *Proc. R Soc. B*, **283**, 1–10.

Knoll, A.H., **Wörndle, S.** and **Kah, L.C.** (2013) Covariance of microfossil assemblages and microbialite textures across an Upper Mesoproterozoic carbonate platform. *Palaios*, **28**, 453–470.

Koch, A.L. and **Ehrenfeld, E.** (1968) The size and shape of bacteria by light scattering measurements. *Biochim. Biophys. Acta*, **165**, 262–273.

Komaristaya, V.P. and **Gorbulin, O.S.** (2006) Sporopollenin in the composition of cell walls of Dunaliella salina Teod. (Chlorophyta) zygotes. *Inter. J. Algae*, **8**, 43–52.

Konhauser, K.O. and **Ferris, F.G.** (1996) Diversity of iron and silica precipitation by microbial mats in hydrothermal waters, Iceland: Implications for Precambrian iron formations. *Geology*, **24**, 323–326.

Konhauser, K.O. and **Urrutia, M.M.** (1999) Bacterial clay authigenesis: a common biogeochemical process. *Chem. Geol.*, **161**, 399–413.

Konhauser, K.O., **Phoenix, V.R.**, **Bottrell, S.H.**, **Adams, D.G.** and **Head, I.M.** (2001) Microbial–silica interactions in Icelandic hot spring sinter: possible analogues for some Precambrian siliceous stromatolites. *Sedimentology*, **48**, 415–433.

Krauskopf, K.B. (1956) Dissolution and precipitation of silica at low temperatures. *Geochim. Cosmochim.*, **10**, 1–26.

Lawson, M., **Sitgreaves, J.**, **Rasbury, T.**, **Wooton, K.**, **Esch, W.**, **Marcon, V.**, **Henares, S.**, **Konstantinou, A.**, **Kneller, E.**, **Gombosi, D.**, **Torres, V.**, **Silva, A.**, **Alevato, R.**, **Wren, M.**, **Becker, S.** and **Eiler, J.** (2023) New age and lake chemistry constraints on the Aptian pre-salt carbonates of the central South Atlantic. *GSA Bulletin*, **135**, 595–607.

Li, F.-S., **Phyo, P.**, **Jacobowitz, J.**, **Hong, M.** and **Weng, J.-K.** (2018) The molecular structure of plant sporopollenin. *Nature Plants*, **5**, 41–46.

Lima, B.E.M. and **De Ros, L.F.** (2019) Deposition, diagenetic and hydrothermal processes in the Aptian Pre-Salt lacustrine carbonate reservoirs of the northern Campos Basin, offshore Brazil. *Sediment. Geol.*, **383**, 55–81.

Liu, J. and **Jiang, Y.** (2018) Multiphase of the meteoric diagenetic environment of carbonates and its relationship with reservoir: a case study of the Jingxi Area in the Ordos Basin, China. *Carbon. Evap.*, **33**, 547–560.

Lohmann, K.C. and **Meyers, W.J.** (1977) Microdolomite inclusions in cloudy prismatic calcites: A proposed criterion for former high-magnesium calcites. *J. Sediment. Res.*, **47**, 1078–1088.

Loucks, R.G. (1999) Paleocave carbonate reservoirs: origins, burial-depth modifications, spatial complexity, and reservoir implications. *AAPG Bulletin*, **83**(11), 1795–1834.

Maliva, R.G., **Knoll, A.H.** and **Siever, R.** (1989) Secular change in chert distribution; a reflection of evolving biological participation in the silica cycle. *PALAIOS*, **4**, 519–532.

Maliva, R.G., **Knoll, A.H.** and **Simonson, B.M.** (2005) Secular change in the Precambrian silica cycle: Insights from chert petrology. *Geol. Soc. Am. Bull.*, **117**, 835–845.

Marin-Carbonne, J., **Robert, F.** and **Chaussidon, M.** (2014) The silicon and oxygen isotope compositions of Precambrian cherts: A record of oceanic paleo-temperatures? *Precambrian Res.*, **247**, 223–234.

Mastalerz, M., Drobniak, A. and Stankiewicz, A.B. (2018) Origin, properties, and implications of solid bitumen in source-rock reservoirs: A review. *Int. J. Coal Geol.*, **195**, 14–36.

Mello, M.R., Rostirolla, S.P., Elias, V., Ferreira, M., Ahualli, A.P., Becker, S., Dahl, J.E. and Moldowan, J.M. (2021) Chapter 2: lacustrine source rocks and oil systems present in the lower cretaceous pre-salt section of the Santos Basin, Brazil. In: *Memoir 124: The Supergiant Lower Cretaceous Pre-Salt Petroleum Systems of the Santos Basin, Brazil* (Eds Mello, M.R., Yilmaz, P.O. and Katz, B.J.), pp. 35–76. AAPG.

Mercedes-Martín, R., Ayora, C., Tritlla, J. and Sánchez-Román, M. (2019) The hydrochemical evolution of alkaline volcanic lakes: a model to understand the South Atlantic Pre-salt mineral assemblages. *Earth Sci. Rev.*, **198**, 1–19.

Misch, D., Gross, D., Hawranek, G., Horsfield, B., Klaver, J., Mendez-Martin, F., Urai, J.L., Vranjes-Wessely, S., Sachsenhofer, R.F., Schmatz, J., Li, J. and Zou, C. (2019) Solid bitumen in shales: Petrographic characteristics and implications for reservoir characterization. *Int. J. Coal Geol.*, **205**, 14–31.

Moore, K.R., Daye, M., Gong, J., Williford, K., Konhauser, K. and Bosak, T. (2023) A review of microbial-environmental interactions recorded in Proterozoic carbonate-hosted chert. *Geobiology*, **21**, 3–27.

Moreira, J.L.P., Madeira, C.V., Gil, J.A. and Machado, M.A.P. (2007) Bacia de Santos. *Boletin Geociencias. Petrobras.*, **12**, 531–549.

Nakano, C.M.F., Pinto, A.C.C., Marcusso, J.L. and Minami, K. (2009) *Pre-Salt Santos Basin – Extended Well Test and Production Pilot in the Tupi Area – the Planning Phase.* Journal of Petroleum Technology, Houston, TX.

Opfergelt, S. and Delmelle, P. (2012) Silicon isotopes and continental weathering processes: Assessing controls on Si transfer to the ocean. *C. R. Geosci.*, **344**, 723–738.

Pietzsch, R., Oliveira, D.M., Tedeschi, L.R., Queiroz Neto, J.V., Figueiredo, M.F., Vazquez, J.C. and de Souza, R.S. (2018) Palaeohydrology of the Lower Cretaceous pre-salt lacustrine system, from rift to post-rift phase, Santos Basin, Brazil. *Palaeogeogr. Palaeoclimatol. Palaeoecol.*, **507**, 60–80.

Pietzsch, R., Tedeschi, L.R., Oliveira, D.M., dos Anjos, C.W.D., Vazquez, J.C. and Figueiredo, M.F. (2020) Environmental conditions of deposition of the Lower Cretaceous lacustrine carbonates of the Barra Velha Formation, Santos Basin (Brazil), based on stable carbon and oxygen isotopes: A continental record of pCO2 during the onset of the Oceanic Anoxic Event 1a (OAE 1a) interval? *Chem. Geol.*, **535**, 119457.

Pikuta, E.V., Hoover, R.B. and Tang, J. (2007) Microbial extremophiles at the limits of life. *Crit. Rev. Microbiol.*, **33**, 183–209.

Rice, C.M., Trewin, N.H. and Anderson, L.I. (2002) Geological setting of the Early Devonian Rhynie cherts, Aberdeenshire, Scotland: an early terrestrial hot spring system. *JGS*, **159**, 203–214.

Riding, R. (Ed) (1991) Classification of microbial carbonates: in Riding, R., ed., Calcareous algae and stromatolites: Springer-Verlag, Berlin, p. 21–51.

Riding, R. (2000) Microbial carbonates: the geological record of calcified bacterial-algal mats and biofilms: *Microbial carbonates. Sedimentology*, **47**, 179–214.

Roadcap, G.S., Sanford, R.A., Jin, Q., Pardinas, J.R. and Bethke, C.M. (2006) Extremely alkaline (pH > 12) ground water hosts diverse microbial community. *Groundwater*, **44**, 511–517.

Rodríguez-Berriguete, Á., Dal' Bo, P.F., Valle, B. and Borghi, L. (2022) When distinction matters: Carbonate shrubs from the Aptian Barra Velha Formation of Brazilian's Pre-salt. *Sedimentary Geology*, **440**, 106236.

Saller, A., Rushton, S., Buambua, L., Inman, K., McNeil, R. and Dickson, J.A.D. (2016) Presalt stratigraphy and depositional systems in the Kwanza Basin, offshore Angola. *AAPG Bulletin*, **100**, 1135–1164.

Samolov, E., Baumann, K., Büdel, B., Jung, P., Leinweber, P., Mikhailyuk, T., Karsten, U. and Glaser, K. (2020) Biodiversity of algae and cyanobacteria in biological soil crusts collected along a climatic gradient in chile using an integrative approach. *Microorganisms*, **8**, 1–28.

Sartorato, A.C.L., Tonietto, S.N. and Pereira, E. (2020) *Silicification and dissolution features in the Brazilian Pre-salt Barra Velha formation: impacts in the reservoir quality and insights for 3D geological modeling.* Rio Oil & Gas Expo and Conference 2020 Proceedings, Rio de Janeiro, Brazil.

Schopf, J.W. (1992) Evolution of the Proterozoic biosphere: bench- marks, tempo, and mode. In: Schopf J.W., Klein, C. (eds) *The Proterozoic biosphere.* Cambridge University Press, New York, pp 583–600.

Schultze-Lam, S., Ferris, F.G., Konhauser, K.O. and Wiese, R.G. (1995) In situ silicification of an Icelandic hot spring microbial mat: implications for microfossil formation. *Can. J. Earth Sci.*, **32**, 2021–2026.

Sergeev, V.N. and Sharma, M. (2012) Proterozoic fossil cyanobacteria. *Palaeobotanist*, **61**, 189–358.

Shapiro, R.S. (2000) A comment on the systematic confusion of thrombolites. *PALAIOS*, **15**, 166–169.

Sharp, Z.D., Gibbons, J.A., Maltsev, O., Atudorei, V., Pack, A., Sengupta, S., Shock, E.L. and Knauth, L.P. (2016) A calibration of the triple oxygen isotope fractionation in the SiO2–H2O system and applications to natural samples. *Geochimica et Cosmochimica Acta*, **186**, 105–119.

Siever, R. (1992) The silica cycle in the Precambrian. *Geochim. Cosmochim.*, **56**, 3265–3272.

Sims, P.A., Mann, D.G. and Medlin, L.K. (2006) Evolution of the diatoms: insights from fossil, biological and molecular data. *Phycologia*, **45**, 361–402.

Strauss, J.V. and Tosca, N.J. (2020) Mineralogical constraints on Neoproterozoic pCO$_2$ and marine carbonate chemistry. *Geology*, **48**, 599–603.

Strullu-Derrien, C., Kenrick, P. and Knoll, A.H. (2019) The Rhynie chert. *Curr. Biol.*, **29**, R1218–R1223.

Strullu-Derrien, C., Le Hérissé, A., Goral, T., Spencer, A.R.T. and Kenrick, P. (2021) The overlooked aquatic green algal component of early terrestrial environments: *Triskelia scotlandica* gen. et sp. nov. from the Rhynie cherts. *Pap. Palaeontol.*, **7**, 709–719.

Teboul, P.-A., Durlet, C., Girard, J.-P., Dubois, L., San Miguel, G., Virgone, A., Gaucher, E.C. and Camoin, G. (2019) Diversity and origin of quartz cements in continental carbonates: Example from the Lower Cretaceous rift deposits of the South Atlantic margin. *Appl. Geochem.*, **100**, 22–41.

Terra, G.J.S., Spadini, A.R. and Franca, A.B. (2009) Carbonate rock classification applied to brazilian sedimentary basins; Classificacao de rochas carbonaticas

aplicavel as bacias sedimentares brasileiras. *Boletim de Geociencias da Petrobras*, **18**, 9–29.

Tissot, B.P. and Welte, D.H. (1984) *Petroleum Formation and Occurrence*. Springer, Berlin Heidelberg, Berlin, Heidelberg.

Tonietto, S.N., Gomes, J.P.B., Bunevich, R.B. and Erthal, M.M. (2023) Spherulitstone as a transitional facies responding to lake level variation? Diagenetic or depositional? In: *Third International Meeting for Applied Geoscience & Energy Expanded Abstracts*, pp. 341–345. Society of Exploration Geophysicists and American Association of Petroleum Geologists, Houston, TX.

Tosca, N.J. and Wright, V.P. (2015) Diagenetic pathways linked to labile Mg-clays in lacustrine carbonate reservoirs: a model for the origin of secondary porosity in the Cretaceous pre-salt Barra Velha Formation, offshore Brazil. *Geol. Soc. London Spec. Publ.*, **435**, 33–46.

Tosca, N.J., Macdonald, F.A., Strauss, J.V., Johnston, D.T. and Knoll, A.H. (2011) Sedimentary talc in Neoproterozoic carbonate successions. *Earth Planet. Sci. Lett.*, **306**, 11–22.

Tutolo, B.M. and Tosca, N.J. (2018) Experimental examination of the Mg-silicate-carbonate system at ambient temperature: Implications for alkaline chemical sedimentation and lacustrine carbonate formation. *Geochim. Cosmochim.*, **225**, 80–101.

Van Den Boorn, S.H.J.M., Van Bergen, M.J., Vroon, P.Z., De Vries, S.T. and Nijman, W. (2010) Silicon isotope and trace element constraints on the origin of ~3.5Ga cherts: Implications for Early Archaean marine environments. *Geochim. Cosmochim.*, **74**, 1077–1103.

Vandenbroucke, M. (2003) Kerogen: from types to models of chemical structure. *Oil & Gas Sci. Technol. Rev.*, **58**, 243–269.

Vázquez-García, B., Ceolin, D., Fauth, G., Borghi, L., Valle, B. and De Moraes Rios Netto, A. (2021) Ostracods from the late Albian–early Cenomanian of the Sergipe–Alagoas Basin, Brazil: New taxonomic and biostratigraphic inferences. *J. South Am. Earth Sci.*, **108**, 103169.

Walter, M.R., Bauld, J. and Brock, T.D. (1972) Siliceous algal and bacterial stromatolites in hot spring and geyser effluents of Yellowstone National Park. *Science*, **178**, 402–405.

Wang, B. and Al-Aasm, I.S. (2002) Karst-Controlled Diagenesis and Reservoir Development: Example from the Ordovician Main-Reservoir Carbonate Rocks on the Eastern Margin of the Ordos Basin, China. *AAPG Bulletin*, **86**, 1639–1658.

Weidlich, O. (2010) Meteoric diagenesis in carbonates below karst unconformities: heterogeneity and control factors. *Geol. Soc. London Spec. Publ.*, **329**, 291–315.

Wood, J.M., Sanei, H., Haeri-Ardakani, O., Curtis, M.E., Akai, T. and Currie, C. (2018) Solid bitumen in the Montney Formation: Diagnostic petrographic characteristics and significance for hydrocarbon migration. *Int. J. Coal Geol.*, **198**, 48–62.

Wright, V.P. (2012) Lacustrine carbonates in rift settings: the interaction of volcanic and microbial processes on carbonate deposition. *Geol. Soc. London Spec. Publ.*, **370**, 39–47.

Wright, V.P. and Barnett, A.J. (2015) An abiotic model for the development of textures in some South Atlantic early Cretaceous lacustrine carbonates. *Geol. Soc. Lond. Spec. Publ.*, **418**, 209–219.

Wright, V.P. and Barnett, A.J. (2017) Critically evaluating the current depositional models for the Pre-Salt Barra Velha Formation, Offshore Brazil. Search and Discovery Article #51439.

Wright, V.P. and Barnett, A.J. (2020) The textural evolution and ghost matrices of the Cretaceous Barra Velha Formation carbonates from the Santos Basin, offshore Brazil. *Facies*, **66**, 7.

Wright, V.P. and Tosca, N.J. (2016) A geochemical model for the formation of the Pre-Salt reservoirs, Santos Basin, Brazil: Implications for understanding reservoir distribution. Search and Discovery Article #51304.

Supporting Information

Additional information may be found in the online version of this article:

Appendix S1. Description of supplemental methods.